

By

A Thesis Submitted to the Faculty of Embry-Riddle Aeronautical University

In Partial Fulfillment of the Requirements for the Degree of

Master of Science in Aerospace Engineering

Embry-Riddle Aeronautical University

Daytona Beach, Florida

*To my family, for always believing in me*

## ACKNOWLEDGEMENTS

I would like to begin this acknowledgements section by expressing my deepest gratitude to my thesis advisor, Dr. Ricklick, for his unwavering guidance, invaluable insights, and continuous support through this research endeavor. Thank you for all the life lessons and the friendship that we have built over the last two years, I will take these with me for the rest of my life. Additionally, I would like to extend my thanks to Dr. Boetcher, for her expertise, advice, and words of encouragement that have helped me to overcome numerous hurdles along the way.

Thank you to all my labmates who made it fun to come to the lab for countless hours of testing and writing: Yang Chao, Nicholas Lopes, Dominic Perito, Devon Hardy, Paula Sanjuan, Adam Duke, Connor Troxler, and Joe Saurbrun. I am very grateful for our friendship and I look forward to see the great things you are going to accomplish in your careers.

To my teammates on the ERAU Men's Basketball team, for helping me to get my mind off work when things were not going as expected and for being my "escape valve" throughout my entire college career.

To my parents and sister, for their unconditional love and for always believing in me, even when I didn't. Your sacrifices, advice, and work ethic have been the cornerstone of my academic and personal growth and have shaped me into the man I am today. I will never be able to express my gratitude and the love I have for you.

And lastly, to my grandparents, for being the best role models that I could have ever had. Your stories of resilience and wisdom and the example that you set for as a kid have taught me the real meaning of toughness and how to never give up, culminating in this master's thesis.

## ABSTRACT

Heat transfer of supercritical carbon dioxide (sCO<sub>2</sub>) was studied experimentally by commissioning a sCO<sub>2</sub> flow loop featuring a horizontal tube-in-tube counterflow heat exchanger with a circular cross section. The main objective was to establish experimental heat transfer research capabilities for sCO<sub>2</sub> at Embry-Riddle Aeronautical University's (ERAU) Thermal Science Lab. sCO<sub>2</sub> experiences a drastic change in thermophysical properties near its critical point that results in unique heat transfer characteristics. The high pressures at which sCO<sub>2</sub> exists make the large gradients in thermophysical and transport properties difficult to study, experimentally and numerically. However, understanding the heat transfer characteristics and thermophysical behavior of sCO<sub>2</sub> is essential in designs taking advantage of these improved heat transfer rates and efficiencies. Traditional correlations for heat transfer of single-phase fluids such as water or oil break down when the nonlinear thermophysical properties of sCO<sub>2</sub> are taken into account. Thus, the fundamental characteristics of sCO<sub>2</sub> heat transfer, as well as its sensitivity to inlet and boundary conditions, must be studied experimentally to validate computational models. The rig developed as part of this work was benchmarked and validated against previous work from the literature.

The designed test section comprised a 0.5 m long test section made up of a copper inner tube with an inner diameter of 6 mm and thickness of 1 mm containing the sCO<sub>2</sub> which was cooled by a water jacket with an inner diameter of 12.7 mm. Temperature measurements were taken at 10 different axial locations along the test section, allowing for the calculation of local and average heat transfer coefficient under different boundary conditions. In addition to the experimental rig, a 1-D computational tool for pretest predictions was created. It was used to determine the operational parameters for the different subsystems in the loop to achieve a steady state, constant heat flux, cooling boundary condition; as well as making sure that the sCO<sub>2</sub> remained within safe

operational conditions governed by the capabilities of the flow loop. The designed rig allows for sCO<sub>2</sub> experiments with testing conditions up to 1,500 psi (10.34 MPa) and 85°C (353.15 K). Cases at pressures between 4 and 9 MPa and mass fluxes up to 220 kg/m<sup>2</sup>s, where tested, with test section inlet temperature ranging between 20°C and 45°C. The experimental results are compared to the ones presented in the literature and the maximum difference for all cases is within 20%.

## TABLE OF CONTENTS

ACKNOWLEDGEMENTS.....	i
ABSTRACT.....	ii
TABLE OF CONTENTS.....	iv
LIST OF FIGURES .....	vii
LIST OF TABLES .....	ix
NOMENCLATURE .....	x
1 Introduction.....	1
1.1 Significance of the Study .....	3
1.2 Statement of the Problem.....	5
1.3 Objectives .....	6
2 Review of the Relevant Literature .....	7
2.1 Power Generation.....	8
2.1.1 Waste-heat Recovery .....	9
2.1.2 Concentrating Solar Power .....	11
2.2 Analytical Studies .....	12
2.2.1 Base Case .....	12
2.2.2 Microchannels and Entrance Effects .....	13
2.2.3 Vertical Flows.....	13
2.2.4 Different Pipe Geometries .....	15
2.2.5 Protuberances and Turbulators .....	15

2.2.6	Real-world Applications .....	16
2.3	Experimental Work.....	17
2.4	Summary .....	29
3	Methodology .....	30
3.1	Experimental Apparatus.....	30
3.1.1	Test Section Design .....	33
3.1.2	Pre-heater and Cooler Modification.....	36
3.1.3	Safety Features.....	37
3.2	Data Collection .....	37
3.3	Data Reduction.....	38
3.4	Uncertainty Analysis.....	40
3.5	Pretest Prediction Code.....	42
3.6	Test Matrix.....	46
3.7	Assumptions Made and Limitations .....	47
3.7.1	Total Heat Transferred Calculations .....	47
3.7.2	Test Section Pressure Drop Calculations .....	48
3.7.3	Cooling and Pump Performance Limitations.....	48
3.7.4	Thermal Buckling and Cyclic Loading.....	49
4	Results and Discussion .....	51
4.1	Analytical Results .....	51

4.1.1	Pretest Prediction Code Output.....	51
4.1.2	Water Mass Flow Effect .....	53
4.1.3	Maximum Heat Flux Study.....	54
4.2	Experimental Results .....	57
4.2.1	Water Loop Heat Leakage .....	57
4.2.2	Accumulator Performance .....	58
4.2.3	Pump and Flow Meter Performance .....	60
4.2.4	Subcritical Validation .....	62
4.2.5	Supercritical Validation .....	64
5	Conclusions and Recommendations .....	67
5.1	Recommendations and Future Work .....	67
6	REFERENCES .....	69
7	PUBLICATIONS.....	73

## LIST OF FIGURES

Figure 1.1 Phase diagram of CO <sub>2</sub> , including the supercritical region ( $T_{pc} = 304.4$ K, $P_{pc} = 7.39$ MPa).....	2
Figure 1.2 Thermophysical and fluid property variations of sCO <sub>2</sub> at $P = 7.4$ MPa, normalized by maximum in-range values.....	2
Figure 1.3 Thermal efficiencies of power conversion systems and applications [5].....	5
Figure 2.1 Potential sCO <sub>2</sub> power cycle layouts: (a) supercritical recuperated; (b) supercritical reheated-recuperated; (c) supercritical recompression; (d) transcritical recuperated. Red lines represent heat-addition and blue heat-rejection [14]. .....	9
Figure 2.2 Comparison between different thermodynamic cycles for waste heat recovery at various temperature-levels and scales [15]. .....	10
Figure 2.3 Schematic diagram of the buoyancy and acceleration effects on sCO <sub>2</sub> vertical flows [25]. .....	14
Figure 2.4 Pitla et al. flow loop schematic [11]. .....	18
Figure 2.5 Liao and Zhao flow loop schematic [31]. .....	20
Figure 2.6 Liao and Zhao test section schematic [31]. .....	20
Figure 2.7 Liu et al. flow loop schematic [32]. .....	22
Figure 2.8 Liu et al. test section schematic [32]. .....	23
Figure 2.9 Zhang et al. flow loop schematic [4]. .....	24
Figure 2.10 Zhang et al. test section schematic [4]. .....	25
Figure 2.11 Dang and Hihara flow loop schematic [21]. .....	27
Figure 2.12 Dang and Hihara test section schematic [21]. .....	28
Figure 3.1 Flow loop schematic. ....	31
Figure 3.2 Flow loop experimental setup. ....	32
Figure 3.3 Schematic of test section. ....	34
Figure 3.4 Test section cross section. ....	34
Figure 3.5 Experimental test section. ....	35
Figure 3.6 Simplified test section model for CFD. ....	36

Figure 3.7 Cooler average heat transfer coefficient ( $h$ ) and actual heat transfer coefficient for the range of operating temperatures ( $h$ ).....	45
Figure 3.8 Preheater average heat transfer coefficient ( $h$ ) and actual heat transfer coefficient for the range of operating temperatures ( $h$ ).....	45
Figure 3.9 Test Section overall average heat transfer coefficient ( $h$ ), mean heat transfer coefficient for each subsection ( $h$ ), and heat transfer coefficient for the range of operating temperatures ( $h$ ).....	46
Figure 3.10 Right side of test section copper tube.....	50
Figure 3.11 Middle of test section copper tube.....	50
Figure 4.1 Change in CO <sub>2</sub> and water temperature with respect to x-location for test section inlet conditions of P = 8 MPa, T = 50°C, d = 6 mm, G = 200 kg/m <sup>2</sup> s, and $q_w'' = 33$ kW/m <sup>2</sup> . ....	53
Figure 4.2 Test section counterflow heat exchanger simulation for different water mass flows ( $m$ ) for test section inlet temperatures of P = 8 MPa, T = 50°C, d = 6 mm, G = 200 kg/m <sup>2</sup> s, and $q_w'' = 33$ kW/m <sup>2</sup> . ....	54
Figure 4.3 Test section counterflow heat exchanger simulation for maximum heat flux cooling case.....	55
Figure 4.4 Test section counterflow heat exchanger simulation for maximum heat flux heating case.....	56
Figure 4.5 $\Delta TH_{20}$ and uncertainty levels for steady-state conditions at a water inlet temperature of 15°C.....	58
Figure 4.6 Flow loop internal pressure variations when accumulator is charged below the recommended pressures.....	59
Figure 4.7 Flow loop internal pressure variations when accumulator is charged inside the recommended values.....	59
Figure 4.8 Gear pump performance under isothermal conditions and different RPM settings for P = 780 psi and T = 22.5°C.....	61
Figure 4.9 CO <sub>2</sub> targeted mass flux (G = 200 kg/m <sup>2</sup> s) recorded by the Coriolis mass flow meter at steady-state conditions.....	62
Figure 4.10 Subcritical results for average heat transfer coefficient ( $h$ ) compared to Gnielinski correlation.....	64
Figure 4.11 Supercritical results for average heat transfer coefficient ( $h$ ) compared to Dang and Hihara correlation.....	66

## LIST OF TABLES

Table 1.1 Characteristics and properties of some refrigerants [8].	4
Table 3.1 Instrumentation accuracy.	41
Table 3.2 Test matrix.	47
Table 4.1 Flow loop operating conditions for test section inlet conditions of $P = 8 \text{ MPa}$ , $T = 50^\circ\text{C}$ , $d = 6 \text{ mm}$ , $G = 200 \text{ kg/m}^2\text{s}$ , and $q_w'' = 33 \text{ kW/m}^2$ .	52
Table 4.2 Subcritical tests results.	63
Table 4.3 Supercritical test results.	65

## NOMENCLATURE

$A$	Area (m <sup>2</sup> )
$CCGT$	Combined Cycle Gas Turbine
$c_p$	Specific Heat (J/kgK)
$\bar{c}_p$	Integrated Specific Heat (J/kgK)
$d$	Diameter (m)
$D_h$	Hydraulic Diameter (m)
$f$	Friction Factor
$G$	Mass Flux (kg/m <sup>2</sup> s)
$h$	Heat Transfer Coefficient (W/m <sup>2</sup> K)
$\bar{h}$	Average Heat Transfer Coefficient (W/m <sup>2</sup> K)
$k$	Thermal Conductivity (W/mK)
$L$	Length (m)
$LMTD$	Logarithmic Mean Temperature Difference (K)
$\dot{m}$	Mass Flow Rate (kg/s)
$Nu$	Nusselt Number
$P$	Pressure (MPa)
$Pr$	Prandtl Number
$q$	Heat Transfer Rate (W)
$q''$	Heat Flux (W/m <sup>2</sup> )
$Re$	Reynolds Number
$s$	Enthalpy (J/kg)
$t$	Thickness (m)

$U$  Overall Heat Transfer Coefficient (W/m<sup>2</sup>K)

$v$  Flow Velocity (m/s)

### **Greek Symbols**

$\Delta$  Change in Property

$\delta$  Uncertainty

$\mu$  Dynamic Viscosity (kg/ms)

$\rho$  Density (kg/m<sup>3</sup>)

$\epsilon$  Pipe Absolute Roughness

### **Subscripts**

1 Inlet

2 Outlet

$b$  Bulk Temperature

$CO_2$  Carbon Dioxide

$f$  Film Temperature

$H_2O$  Water

$pc$  Pseudocritical

$w$  Wall

## 1 Introduction

In recent years, the pursuit of sustainable and efficient energy and propulsion systems has become a paramount global concern. Conventional energy sources and refrigerants are starting to raise environmental challenges resulting in an increasing number of international agreements to limit their impact. Supercritical carbon dioxide has emerged as a promising working fluid in various fields due to its unique thermodynamic properties and potential for heat transfer applications.

When  $s\text{CO}_2$  is heated and pressurized above its critical point, the line separating gas and liquid states fades away, resulting in a state where both gas and liquid properties are present. Figure 1.1 shows the phase diagram for  $s\text{CO}_2$ , with its corresponding states. When supercritical state is reached, carbon dioxide undergoes large changes in thermophysical properties such as increased density, higher diffusivity, and enhanced heat capacity, rendering it a versatile fluid for various industrial applications including extraction and heat transfer. Figure 1.2 shows the large gradient in thermophysical properties near its critical point. Due to this drastic variation in properties,  $s\text{CO}_2$  presents a unique heat transfer behavior different than observed in subcritical flows, providing an advantage in a variety of applications. Additionally,  $\text{CO}_2$  supercritical state ( $31.3^\circ\text{C}$  and  $7.39\text{ MPa}$ ) is easily achievable when compared to other supercritical fluids like water ( $374.2^\circ\text{C}$  and  $22.114\text{ MPa}$ ) [1].  $s\text{CO}_2$  is a natural substance that is benign to the environment and has a small physical footprint, establishing it as a sustainable alternative for a wide range of heat transfer applications, such as power generation, commercial refrigeration, and industrial processes.

The objective of this thesis is the design and benchmarking of a  $s\text{CO}_2$  closed flow loop that establishes heat transfer research capabilities for  $s\text{CO}_2$  at ERAU's Thermal Science lab. The constructed flow loop was designed and validated according to previous experimental work from

the literature and further corroborated with analytical prediction codes and computational fluid dynamics (CFD) simulations. The proposed work will serve as the foundation for future experiments that will allow to study the heat transfer behavior of sCO<sub>2</sub> under a wide range of inlet and boundary conditions.

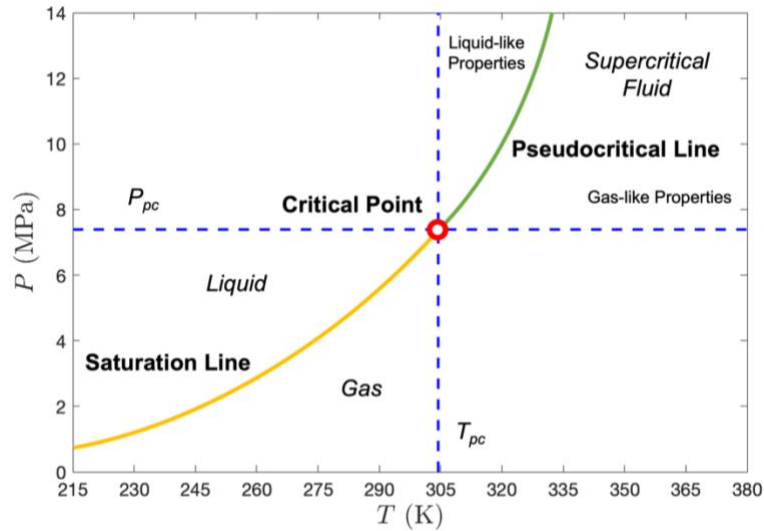


Figure 1.1 Phase diagram of CO<sub>2</sub>, including the supercritical region ( $T_{pc} = 304.4$  K,  $P_{pc} = 7.39$  MPa).

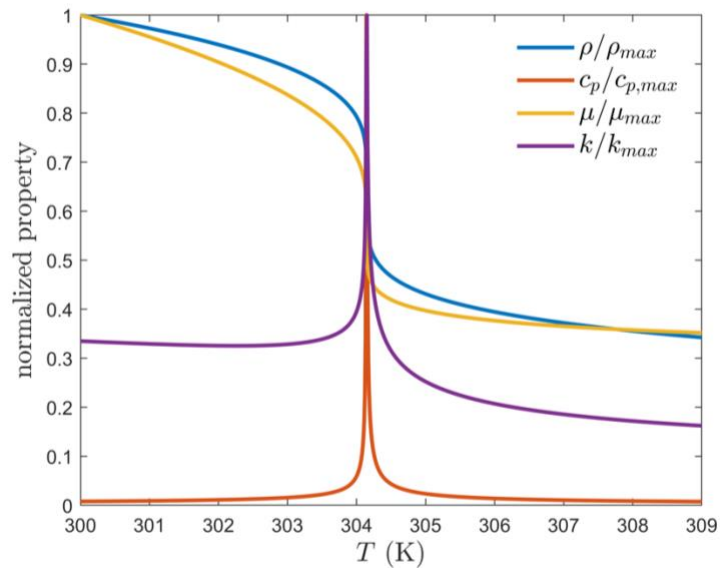


Figure 1.2 Thermophysical and fluid property variations of sCO<sub>2</sub> at  $P = 7.4$  MPa, normalized by maximum in-range values.

## 1.1 Significance of the Study

Supercritical CO<sub>2</sub> finds diverse applications in fields ranging from power generation to refrigeration systems due to its exceptional heat transfer properties, facilitating efficient energy conversion and extraction processes. Despite its promising attributes, sCO<sub>2</sub> has not been thoroughly characterized, particularly its behavior under varying conditions. The study of the heat transfer capabilities of sCO<sub>2</sub> remains an ongoing endeavor, presenting avenues for further research and optimization in numerous industrial and scientific domains.

Currently, CFCs (chlorofluorocarbons) and HCFCs (hydrofluorocarbons) are the most commonly used refrigerants but cause serious environmental damage and ozone depletion [2]. New international laws to promote the use of natural working fluids (NWF) for sustainable refrigeration like the European F-gas regulation EU 517/2014; thus, new alternatives are to be found and implemented [3]. Supercritical carbon dioxide has been deemed as the most promising alternative to these solvents and refrigerants due to its zero Ozone Depletion Potential (ODP) and almost negligible Global Warming Potential (GWP), high solubility, and advantageous thermophysical properties at the critical point [4]. Table 1.1 shows some of the advantages of sCO<sub>2</sub> with respect to other common CFCs and HCFCs.

In addition, sCO<sub>2</sub> has been proposed as a working fluid on several novel power cycles, with special emphasis on next generation nuclear reactors and waste heat recovery systems; sCO<sub>2</sub> Brayton cycles can result in 10 times smaller turbomachinery than steam Rankine cycles due to their high fluid density throughout the whole cycle while also providing gains in thermal efficiency as shown in Figure 1.3 [5]. sCO<sub>2</sub> power cycles present a reduction in the number of stages and the ability to use a single body design, eliminating the need for high, medium, and low-pressure turbines to power the compressor [6]. Renewable energies would also benefit from the usage of supercritical carbon dioxide, further emphasizing the environmental benefits of sCO<sub>2</sub>. For

instance, Concentrating Solar Power (CSP) systems would see an enhancement in efficiency between 5% and 10% by using different sCO<sub>2</sub> power cycles [7]. Additionally, sCO<sub>2</sub> power cycles have a large power scalability (10 MW to multi-100 MW), making them suitable for a broad spectrum of power generation applications, while being more economical due to the smaller turbomachinery and simple cycle designs [7]. This performance improvement and reduced cost would increase the viability of renewable energy sources while reducing greenhouse gas emissions.

*Table 1.1 Characteristics and properties of some refrigerants [8].*

<b>Refrigerant</b>	<b>CFC12</b>	<b>HCFC22</b>	<b>HFC134a</b>	<b>CO<sub>2</sub></b>
<b>Natural Substance</b>	No	No	No	Yes
<b>ODP</b>	1.0	0.05	0	0
<b>GWP – 100 years</b>	7,100	1,500	1,200	1
<b>– 20 years</b>	7,100	4,100	3,100	1
<b>Flammable or explosive</b>	No	No	No	No
<b>Toxic/irritating decomposition products</b>	Yes	Yes	Yes	No
<b>Approx. relative price</b>	1	1	3-5	0.1
<b>Molar mass</b>	120.92	86.48	102.03	44.01

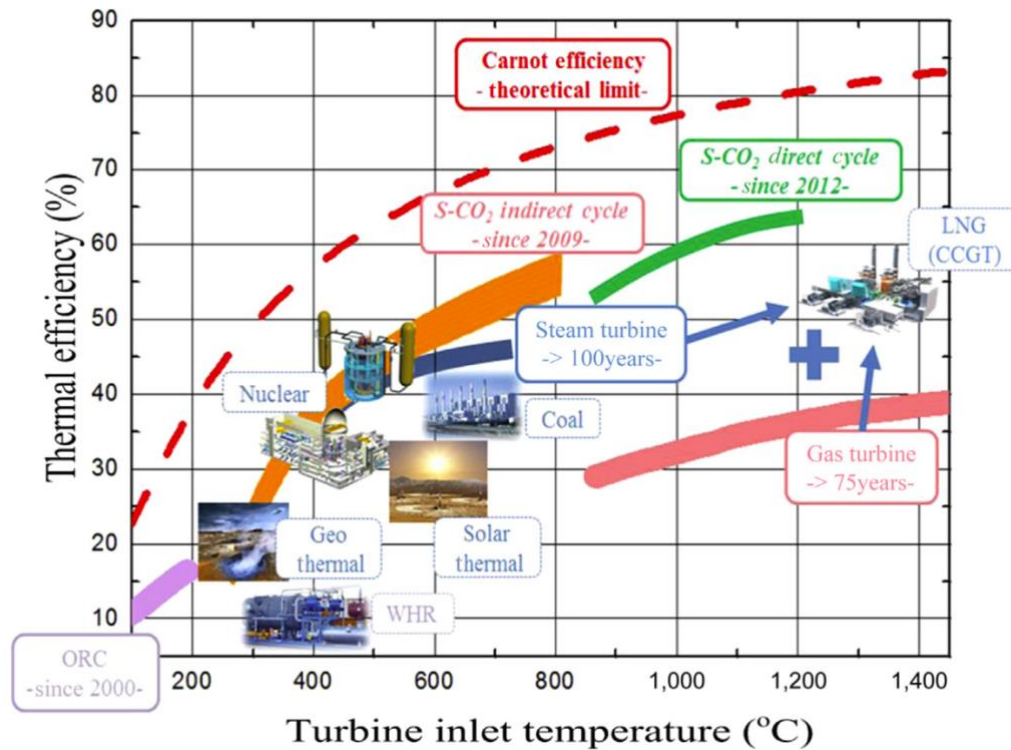


Figure 1.3 Thermal efficiencies of power conversion systems and applications [5].

## 1.2 Statement of the Problem

Carbon dioxide reaches its supercritical state when it is subjected to high temperatures and pressures above its critical point. At this state, sCO<sub>2</sub> displays superior heat transfer capabilities not seen in conventional working fluids, enabling efficient energy conversion and enhancing thermodynamic performance.

All this potential also comes with a great degree of difficulty when it comes to understanding its behavior and properties; around the critical point, small variations in pressure cause large gradients in thermophysical properties. A strong fundamental understanding of heat transfer characteristics is needed to use sCO<sub>2</sub> properly and efficiently in all its potential applications. The influence of fluid property variations around its critical point has been studied experimentally and tried to be replicated numerically by modifying existing correlations like Dittus-Boelter or

Gnielinski [9]. Computational models use these correlations to predict the sCO<sub>2</sub> behavior in different applications and under different conditions. The hypersensitive nature of sCO<sub>2</sub>'s thermophysical properties to pressure and temperature around its critical and pseudocritical points makes it difficult to study using computational models; and models already developed need to be validated experimentally to ensure accuracy. Furthermore, drastic sensitivities to inlet temperatures and boundary conditions, as well as test section geometries, have been observed in the literature and still need to be verified experimentally [10]. While a great deal of research has been performed to determine the heat transfer and pressure drop characteristics of subcritical heat transfer fluid and single-phase coolants, comparatively few investigations have been conducted on the in-tube heat transfer and pressure drop behavior of supercritical fluids [11]. Thus, experimental capabilities for supercritical CO<sub>2</sub> are necessary in order to verify CFD models for a wide range of operating conditions and geometries.

### **1.3 Objectives**

The goal of the current work is to benchmark and validate a sCO<sub>2</sub> flow loop featuring a horizontal tube-in-tube counterflow heat exchanger with circular cross section against the work from the literature; establishing heat transfer research capabilities for sCO<sub>2</sub> at ERAU's Thermal Science Lab. Analytical prediction codes and CFD analysis will accompany the experimental set up to help govern the design and further uphold the validity of the data. Furthermore, the modular design of the flow loop will allow for the test section to be replaced by different designs, allowing for novel experiments to be run in order to collect new data and formulate new correlations. The proposed work will serve as the foundation to verify computational models under a wide range of inlet and boundary conditions, which will play a key role in the future of sCO<sub>2</sub> as a refrigerant and the performance optimization of sCO<sub>2</sub> power cycles and other thermal management applications.

## 2 Review of the Relevant Literature

Over the past several years, there has been a significant number of numerical and experimental studies dedicated to investigating the rapidly changing properties of  $s\text{CO}_2$  around its critical point. In order to take advantage of all of the potential heat transfer applications of  $s\text{CO}_2$  and create effective designs, it is necessary to understand its behavior and properties as well as their effect on the heat transfer behavior. Correlations are needed to compute the Nusselt number, which is the ratio of convective to conductive heat transfer and allows for convective thermal analysis of the fluid. The typical heat transfer correlations used for conventional working fluids and single-phase coolants fail to model the behavior of supercritical  $\text{CO}_2$  when its nonlinear thermophysical properties are considered. The key to govern the performance of  $s\text{CO}_2$  is to improve the accuracy of these correlations and to be able to use them in an efficient way.

The heightened sensitivity of  $s\text{CO}_2$  physical properties along its pseudocritical line has led experts to collect data since the 1950s while generating new correlations applicable to a wider variety of inlet and boundary conditions. However, there is still a lack of consistency on the correlations used to verify numerical models, and modern correlations are only applicable under relatively small ranges of operating conditions [12]. The proposed work will serve as the foundation for further investigation of the fundamental flow physics and heat transfer capabilities of  $s\text{CO}_2$ , which will allow scientists to fully understand and take advantage of all its potential applications as a refrigerant, working fluid for power generation cycles, and other thermal management applications. This section will focus on reviewing the current state of research and development of  $s\text{CO}_2$  in three main areas: power generation, analytical studies, and experimental work.

## 2.1 Power Generation

Power cycles using supercritical carbon dioxide as the working fluid started to be studied in the 1960s. However, after the initial excitement created by its theoretical performance, the number of studies in this field started to decline in favor of standard combustion gas turbines [13]. In the last couple of decades, the interest in these cycles has returned due to its applicability and high efficiency in a variety of power cycles such as Concentrated Solar Power, Waste Heat Recovery and Gen IV nuclear reactors. The main advantage of sCO<sub>2</sub> cycles is that they combine the advantages of steam Rankine cycles and gas turbines. As shown in Figure 1.2, when the temperature of the sCO<sub>2</sub> is brought down past its critical point the fluid becomes more viscous and liquid-like, substantially reducing the compression work required. Additionally, sCO<sub>2</sub> is less corrosive than steam, allowing for higher turbine inlet temperature (TIT) while avoiding material concerns. sCO<sub>2</sub> cycles are similar to steam Rankine cycles in terms of layout but the component design process is comparable to the one for a gas turbine system [5]. The baseline cycle for most studies is the simple recuperated cycle shown in Figure 2.1 (a). On this cycle, a recuperator is used to transfer heat from the hot turbine exhaust to the cold fluid at the exit of the compressor [15]. The sCO<sub>2</sub> Brayton recuperated cycle and similar layouts (Figure 2.1), allow to recover the excess heat created by lower pressure ratios and high TIT when compared to the steam Rankine cycle, increasing the thermal efficiency of the system.

Currently, Sandia National Lab (SNL, New Mexico, USA), Knolls Atomic Power Lab (KAPL, New York, USA), Institute of Applied Energy (IAE, Kyoto, Japan), Korea Advance Institute of Science and Technology (KAIST, Korea), and Korea Institute of Energy Research (KIER, Korea) lead the international effort to study sCO<sub>2</sub> Brayton cycles at lab scale for their potential application on next generation nuclear reactors [5]. Most of their work focuses on integral system testing involving turbomachinery and heat exchangers, as well as performance studies on different cycle

layouts under different operating conditions. However, to evaluate the potential commercial applicability of sCO<sub>2</sub> Brayton cycles and demonstrate their high efficiency, the development of large scale (>10 MW) system prototypes is necessary, becoming the main research focus of the sCO<sub>2</sub> power generation industry.

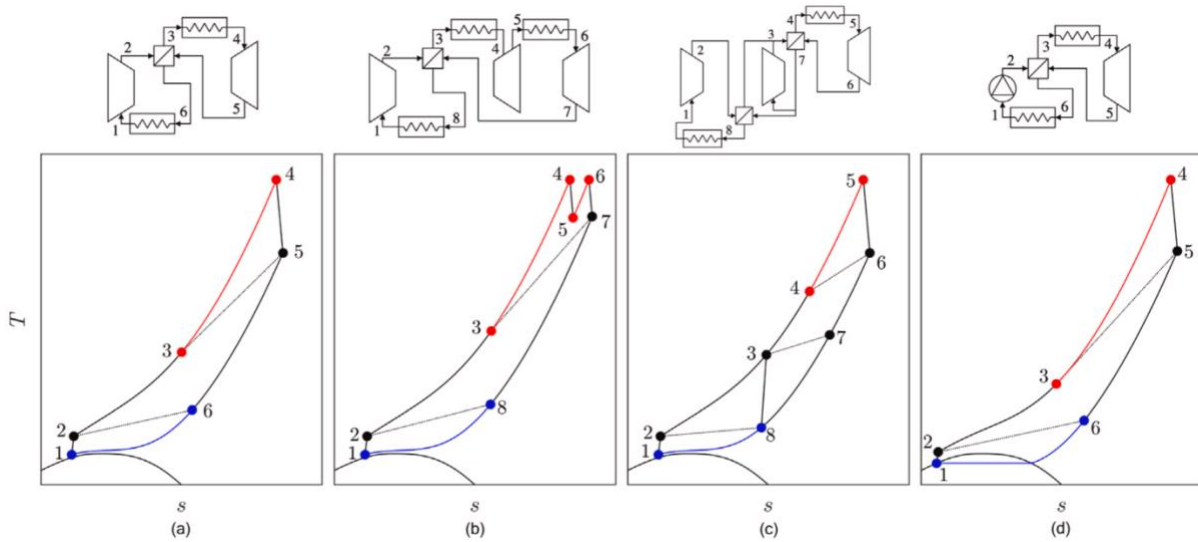


Figure 2.1 Potential sCO<sub>2</sub> power cycle layouts: (a) supercritical recuperated; (b) supercritical reheated-recuperated; (c) supercritical recompression; (d) transcritical recuperated. Red lines represent heat-addition and blue heat-rejection [14].

### 2.1.1 Waste-heat Recovery

Every energy conversion process has losses which come from different sources. The efficiency of these power cycles relies on the ability to minimize or recycle these losses. The main type of energy loss is waste heat. The waste heat resulting from the energy conversion cycles is discharged into the environment contributing to atmospheric pollution and throwing away vast amounts of potential energy. One of the main focuses of the power generation industry is converting this waste heat into useful power through different thermodynamic cycle layouts. Different technical features of sCO<sub>2</sub> power cycles, underscore their suitability for waste heat recovery systems. Firstly, their

compact design allows for adaptable on-site configurations, minimizing investment expenses. Additionally, their comparatively superior cycle efficiency facilitates heightened power generation with reduced thermal energy input; while their capability to accommodate a wide spectrum of heat source temperatures enables the utilization of waste heat recovery for an ampler range of applications. As it can be seen on Figure 2.2, the range of waste heat recovery temperatures for CO<sub>2</sub> cycles is bigger than for steam-based Rankine cycles which are proved to only be efficient for high source temperatures. Lastly, the decreased water consumption and greenhouse gas emissions offer considerable environmental advantages while enhancing the competitiveness of waste heat recovery units [15].

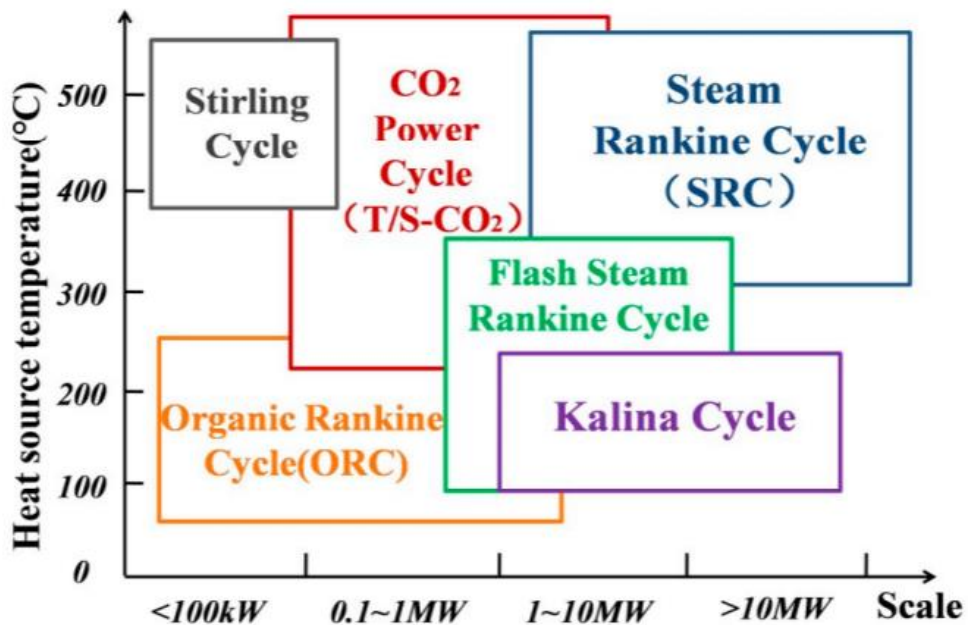


Figure 2.2 Comparison between different thermodynamic cycles for waste heat recovery at various temperature-levels and scales [15].

sCO<sub>2</sub> cycles have already been used to recover the waste heat of different applications. For instance, Sanchez et al. used sCO<sub>2</sub> to recover waste heat from Solid Oxide Fuel Cells (SOFC) and Molten-carbonate Fuel Cells (MCFC) [16], Walnum et al. (Norway) used it for gas turbines for oil and gas production platforms [17], Shu et al. (China) used it to recover the waste heat from internal combustion engines exhaust [18], and Want et al. (China) used sCO<sub>2</sub> to recover waste heat from nuclear reactors [19]. However, these kinds of systems still face different technical challenges that need to be addressed before they are widely implemented.

### **2.1.2 Concentrating Solar Power**

The previously mentioned high power density and large power scalability of sCO<sub>2</sub> power cycles along with their low cost and simple cycle design, makes them ideal candidates for CSP applications. Currently, CSP plants use oil, salt, or steam as heat transfer fluids to carry the energy from the receiver to the turbine-generator system. Turchi et al. [7] present a thermodynamic analysis of supercritical carbon dioxide power cycles used in Concentrating Solar Power systems. It was found that sCO<sub>2</sub> cycles can achieve efficiencies greater than 50%, when compared to subcritical Rankine and Stirling cycles with thermal-to-electric conversion efficiencies ranging between 35% and 40% [7]. Additionally, these cycles are able to accommodate the use of dry cooling, reducing maintenance costs and allowing for the installation of CSP plants in locations where water resources are not abundant. Due to the higher fluid density, sCO<sub>2</sub> turbomachinery would become more compact and would require adding a compressor or reheat stage, increasing the complexity of the cycle design. However, modern multistage axial-flow gas or steam turbines present an even higher degree of complexity. Hence, the improvement in performance and efficiency can substantially surpass the added costs coming from more complex compressor/turbine designs. Turchi et al. [7] conclude that despite the additional intricacy, sCO<sub>2</sub> cycles for CSP applications would enhance cycle performance, while reducing the required sizes

of solar collectors and thermal energy storage systems. Reducing the cost and increasing the efficiency of CSP systems would promote the use of renewable energies and mitigate greenhouse emissions.

In order to clearly understand the viability of sCO<sub>2</sub> for thermal management applications and power cycles, analytical and experimental studies are required. The following two sections will put emphasis on reviewing relevant literature in these two areas.

## **2.2 Analytical Studies**

When performing CFD studies with sCO<sub>2</sub>, there are a number of factors that affect the heat transfer performance of sCO<sub>2</sub>, such as flow tube diameter, heat flux, mass flux, pressure difference, flow orientation, and tube cross sectional geometry. The following subsections highlight certain studies involving different areas of interest regarding the analytical study of the heat transfer properties sCO<sub>2</sub>.

### **2.2.1 Base Case**

When analyzing the heat transfer behavior of sCO<sub>2</sub> analytically, the most common case of study is a horizontal water-cooled counter-flow tube-in-tube heat exchanger. Li et al. [20] propose a 3D RANS model to simulate the experimental set-up proposed by Dang and Hihara [21], studying the heat transfer performance of sCO<sub>2</sub> in a tube-in-tube horizontal heat exchanger under different boundary and inlet conditions. This experimental set up will be explained in the following section of this thesis. Their simulation indicates that the heat transfer coefficient increases with increasing mass flow rate and inlet temperature, while it decreases along the flow direction in the test section due to the decrease in temperature difference between the CO<sub>2</sub> and the water jacket. Additionally, 3-dimensional flow behavior is analyzed, determining that secondary flows appear inside of the heat exchanger creating a spiral pattern that brings the core hot fluid to the walls and results in longer flow paths, enhancing the sCO<sub>2</sub> heat transfer [20]. The paper concludes that these

helical flows are a product of the buoyancy effects created by the different densities between the top and the bottom of the tube cross section.

### **2.2.2 Microchannels and Entrance Effects**

Other numerical studies focus on the entrance effects on the test section. This kind of simulations explore the effect of the development length on the heat transfer behavior of sCO<sub>2</sub>. Adding an adiabatic section before the heated/cooled section ensures that the boundary layer does not affect the heat transfer properties of the fluid. Liu et al. [22] numerically study the entrance effects and length of adiabatic section required in order to have fully developed flow at the entrance of the test section for vertical mini tubes with ID of 0.0992 mm. As the adiabatic section becomes larger, the heat transfer deterioration caused by undeveloped flow moves towards the inlet of the test section and eventually disappears. On the other hand, the shorter the length of the adiabatic section, the greater the fluctuations of the local wall temperature and local convective heat transfer coefficient, resulting in increased heat transfer deterioration [22].

It was concluded that the length of the adiabatic section has a big influence on the convective heat transfer properties of sCO<sub>2</sub>; and that the deterioration range is bigger for low Reynolds numbers and high heat fluxes with shorter adiabatic sections. ERAU has also performed research work in this field, as Chao et al. [23, 24] numerically investigated the effect of hydraulic development length and thermal boundary conditions on local sCO<sub>2</sub> heat transfer.

### **2.2.3 Vertical Flows**

Other analytical studies focus on creating correlations to properly model the buoyancy and acceleration effects on sCO<sub>2</sub> vertical flows. Liu et al. [25] redefined the dimensionless buoyancy and acceleration parameters and their corresponding thresholds for vertical flows. Under heating conditions, convective heat transfer is enhanced when turbulence, caused by shear stress in the boundary layer, appears in the viscous sub-layer. For upward flow, the fluid's buoyancy reduces

the shear stress at the wall resulting on heat transfer degradation. On the other hand, for downward flow, the buoyancy effect increases the shear stress in the boundary layer and the corresponding turbulent mixing in the viscous sub-layer, enhancing convective heat transfer. The acceleration effect reduces the shear stress and dampens the turbulence levels in the boundary layer for both upward and downward flow, reducing the convective heat transfer. Figure 2.3 shows a schematic of a supercritical upwards flow under heating conditions with its corresponding buoyancy and acceleration effects.

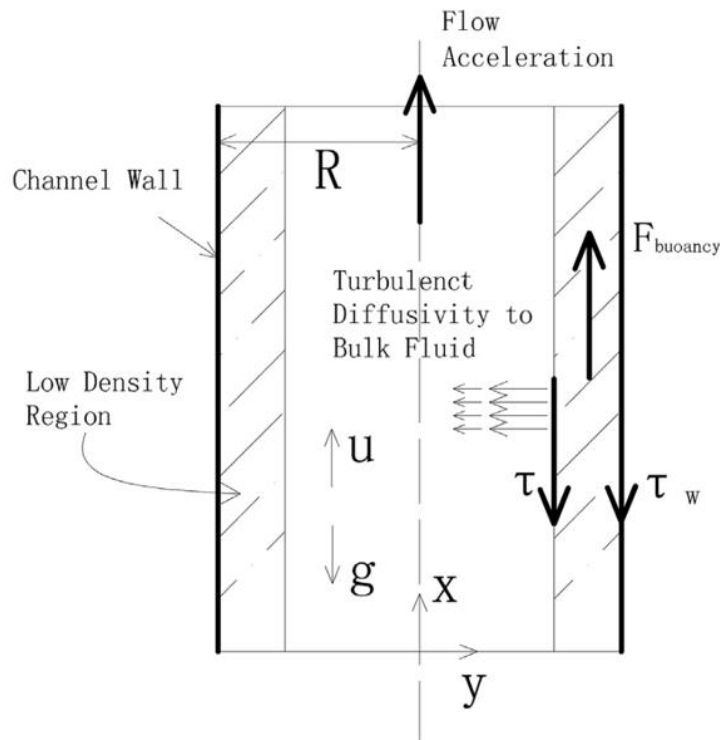


*Figure 2.3 Schematic diagram of the buoyancy and acceleration effects on  $sCO_2$  vertical flows [25].*

#### **2.2.4 Different Pipe Geometries**

Other non-circular cross-sections are studied numerically. Sharabi et al. [26] perform a CFD analysis on triangular and square tube-in-tube heat exchangers with upward flow under heating conditions. The mixed convection case is compared to other two idealized cases (frozen properties, and no gravity) in order to understand the factors that affect heat transfer deterioration of sCO<sub>2</sub>. The flow velocity redistribution caused by the buoyancy effect was found to be the main cause of heat transfer degradation. The deformation of the velocity profile is caused by the differences in fluid density throughout the pipe's cross-section. The fluid temperature near the corners increases due to the greater heat per unit volume coming into the fluid and the decreasing trend in velocity towards the corners near the critical point [26]. These differences in fluid temperature result in different densities throughout the pipe's cross-section which create a deformation of the velocity profile. Thus, the higher temperatures in this region increase the buoyancy effects and cause a reduction in turbulence, resulting in heat transfer degradation at the pseudocritical point.

#### **2.2.5 Protuberances and Turbulators**

Heat transfer enhancement techniques can also be applied to sCO<sub>2</sub> heat exchangers. Li et al. [27] compares different types of heat transfer enhancement techniques (protrusion, dimples, twisted tape insert, coil, fins, groove, rough element...) and uses different expressions to evaluate their efficiencies based on experimental and analytical data from the literature. A new parameter is used to evaluate the enhancement efficiency of a certain enhancement method, reflecting the heat transfer gain against the increment in friction factor [27]. The performance of each of the techniques if evaluated based on Reynolds number, and different heat transfer enhancement methods are proposed for different values of  $Re$ . Additionally, a MATLAB code is developed to optimize the different methods based on Nusselt number and friction factor correlations. Lastly, Liu et al. [27] introduce nano-coating as an additional feature that could be added to any of the

previous enhancement techniques for sCO<sub>2</sub> heat exchangers, resulting in further heat transfer augmentation and drag reduction. However, there is a lack of analytical and experimental data to quantify its effectiveness and performance.

### **2.2.6 Real-world Applications**

Several studies focus on the design of specific components for different sCO<sub>2</sub> applications. As previously mentioned, one of the biggest applications for supercritical carbon dioxide is power generation, especially its potential use as the working fluid for Brayton cycles. Thus, in order to comprehend the viability of this kind of cycles it is important to analyze the behavior of the different components under the new working conditions. Schmitt et al. [28] performed a CFD study on the first stage turbine vane of a 100 MW sCO<sub>2</sub> Brayton cycle with a 1,350 K turbine inlet temperature (TIT). As expected, the high pressure and density of the sCO<sub>2</sub> could cause design complications. The high pressure necessary to maintain the fluid at supercritical state will create big stresses on the turbine blades and the corresponding casing, requiring strong materials and thick housing walls. Additionally, as addressed on previous sections, the high fluid density allows for smaller turbomachinery reducing the overall size of the energy cycle. However, if the size of the turbine blades becomes too small, aerodynamic losses appear in form of tip losses and secondary flows [28]. The manufacturing process of such small blades would be much more complicated and expensive, especially considering the need for internal cooling channels due to the high operational temperatures of the turbine's first stage. It is concluded that bigger sizing would be required in order to increase the blade sizes, correspondingly increasing the power output of the cycle. Designing components for sCO<sub>2</sub> operation may pose greater challenges than for conventional air or steam cycles, thus necessitating further research and innovation to attain the performance flexibility seen in modern gas turbines.

### 2.3 Experimental Work

Since the late 1950s, a number of researchers have conducted numerous investigations to experimentally analyze the rapidly changing thermophysical properties of sCO<sub>2</sub> around its critical point and their impact on flow behavior. These experimental results are necessary to validate computational models and to create new correlations applicable to a wider range of inlet and boundary conditions. In 1957, Bringer et al. [29], performed one of the first experiments using a supercritical CO<sub>2</sub> closed circuit featuring a 24.0 in. Inconel test section with a 0.25 in. OD and a thickness of 0.035 in. The sCO<sub>2</sub> is heated in the test section and cooled in a heat exchanger. The heat flux is applied by method of electrical heating where the current is passed directly through the Inconel wall, achieving values between 10,000 to 100,000 BTU/(hr)(ft<sup>2</sup>). 15 T-type spot-welded thermocouples measured the outer wall temperature, allowing for the calculation of the heat transfer coefficient of the CO<sub>2</sub>. The loop operated at a pressure of 1,200 lb/in<sup>2</sup> and temperatures between 70 to 120°F. They concluded that the existing empirical and semi-empirical correlations fail to predict the behavior of CO<sub>2</sub> when its supercritical state is reached [29]. This is one of the first experiments to observe the rapidly changing properties of sCO<sub>2</sub> with temperature and explore the region of applicability of the existing correlations. Since then, new correlations have been developed in hopes of modeling the behavior of sCO<sub>2</sub> for different geometries and working conditions, leading to a bigger region of applicability.

Pitla et al. [11] conducted an experiment including a horizontal heat exchanger configuration made up of 8 subsections connected in series, five of them being 1.8 m long and the remaining three 1.3 m long; all of them with a 4.7 mm ID. Each subsection constitutes an individual tube-in-tube counterflow heat exchanger where the CO<sub>2</sub> flows in the internal tube and is cooled down by a water jacket. Heat fluxes between 40 to 70 kW/m<sup>2</sup> were used for the experiment and the pressure was kept between 8.0 MPa and 12.0 MPa. The CO<sub>2</sub> bulk temperature at the inlet and outlet of each

subsection is measured by T-type thermocouples placed in the centerline of the flow while thermistors were used to measure the water temperature come in and out of each one of them. Inside of the loop, a sub-cooler using water-glycol brings the CO<sub>2</sub> temperature to about 5°C in order to obtain a liquid-like state with higher viscosity for the CO<sub>2</sub> to be pumped by a variable speed internal gear pump, and a micromotion mass flow meter is used to assure that the desired mass flow was coming into the test section. An electric heater brings the temperature back up to 120°C to achieve supercritical state inside the test section [11]. Figure 2.4 represents the flow loop configuration for the experiment.

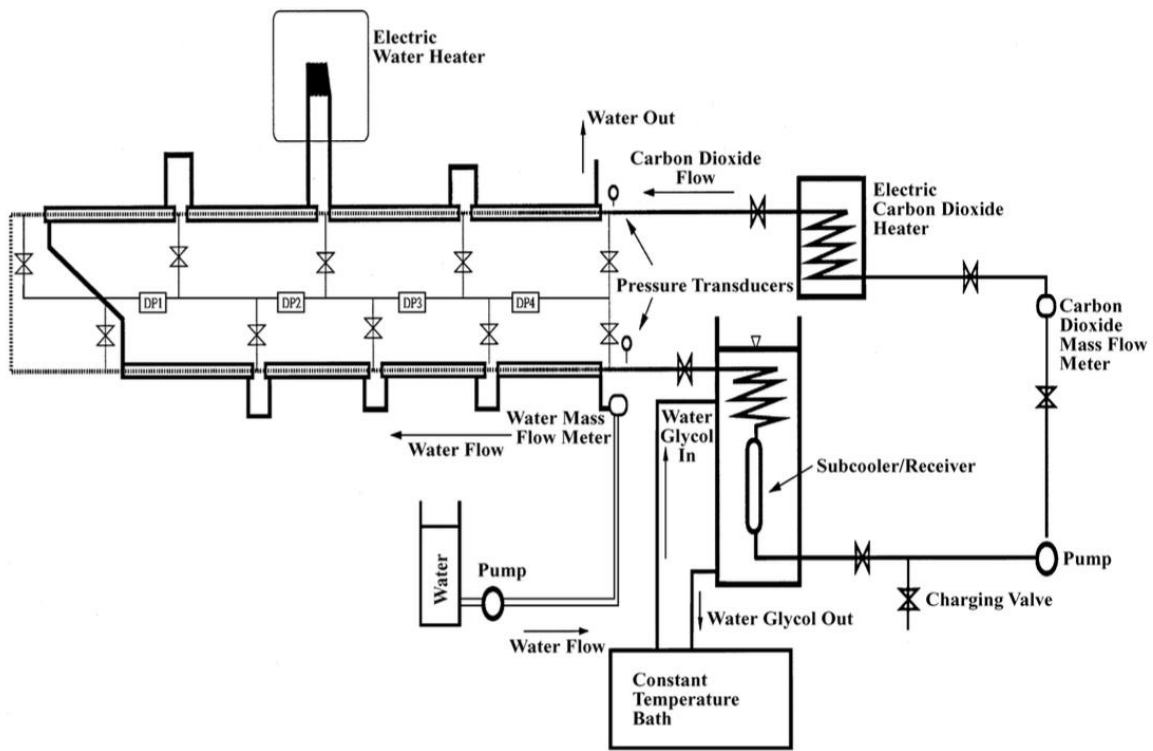


Figure 2.4 Pitla et al. flow loop schematic [11].

Their study underlines the over prediction of Krasnoshchekov and Protopopov [30] model around the critical point and propose a new model based on their experimental results. Additionally, they compare the heat transfer performance of sCO<sub>2</sub> to a common refrigerant like R-22, currently phased out in the US due to its ODP and high GWP. The heat transfer coefficient in the gas cooler is found to be considerably higher than R-22 while also having a lower friction factor [11].

Liao and Zhao [31] conducted several experiments with different flow orientations using miniature circular tubes with 0.70 mm, 1.4 mm, and 2.16 mm ID under heating conditions and mass flows between 0.02 and 0.2 kg/min. By using a constant temperature boundary condition, the effects of buoyancy were explored for horizontal, upward, and downward flow. The effect of pressure, tube diameter, and heat flux on heat transfer performance was also studied. The tubes used for the experiment were stainless steel AISI 304 and had ODs of 1.10 mm, 3.18 mm, and 3.18 mm respectively. The stainless-steel tube was inserted into a 110.0 mm long copper cylinder with a 25 mm OD. The test section was heated through an electrical resistance wire wrapped around the copper. Figure 2.6 shows the test section set up as well as the insulation used; isinglass around the copper cylinder to electrically insulate the copper from the resistance wire and fiber glass wool to thermally insulate the test section from the ambient conditions. There are two thermally insulated segments before and after the test section with lengths of 110.0 mm and 40.0 mm respectively. 6 T-type thermocouples are placed inside a metal oxide silicone oil paste in between the stainless steel and the copper tubes, allowing for the measurement of the outer wall temperature. Two more armored T-type thermocouples are placed at the inlet and outlet of the test section. A pressure gauge transducer measures the inlet pressure of the test section, ranging between 74 to 120 bar for the experiment. A differential pressure transducer measures the pressure

drop across the test section. The rest of the loop is set in a similar way as Pitla et al. experiment [11]. An after-cooler reduces the CO<sub>2</sub> temperature after the test section and feeds the cold, denser, fluid into a Coriolis mass flow meter which sends feedback to regulate the performance of the CO<sub>2</sub> pump. A pre-heater brings the sCO<sub>2</sub> temperature up to the desired testing temperatures, designated to be between 20 and 110°C. The loop set up can be observed in Figure 2.5.

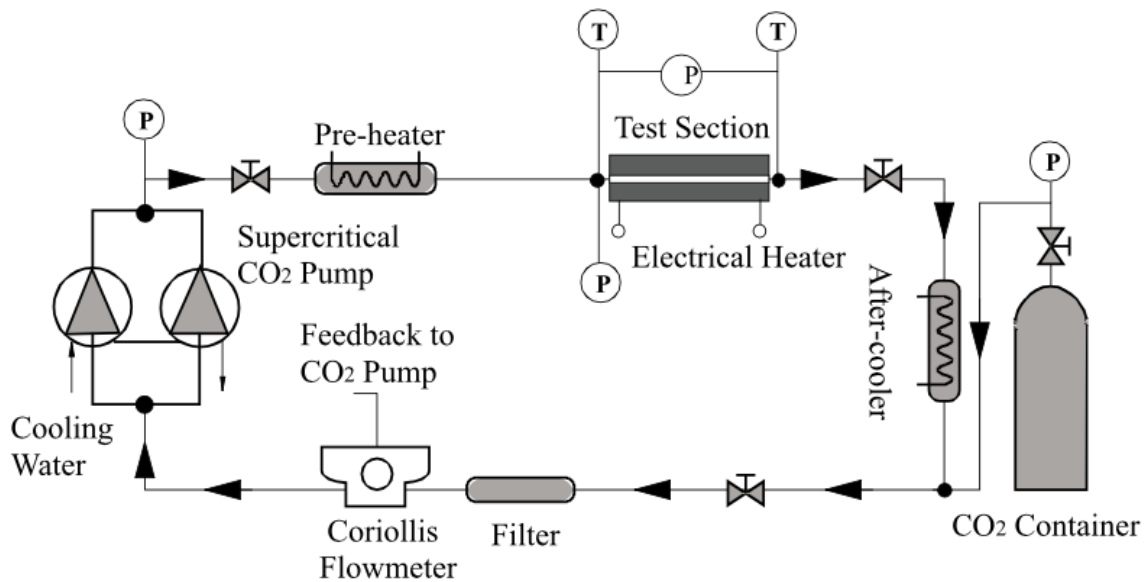


Figure 2.5 Liao and Zhao flow loop schematic [31].

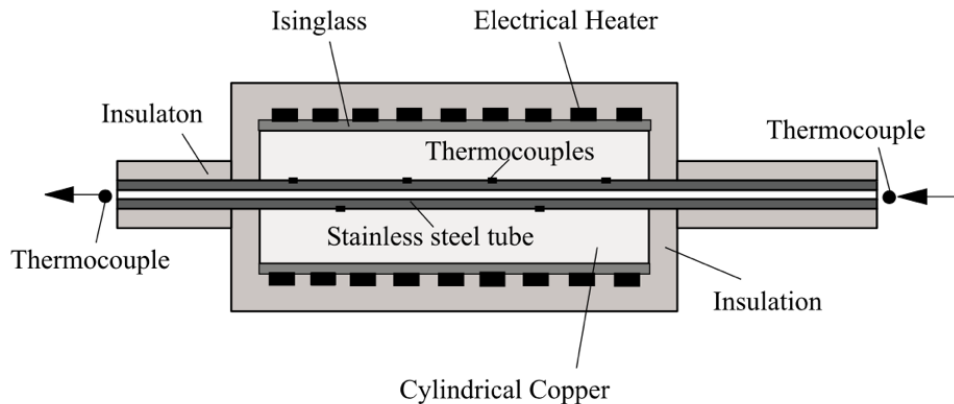


Figure 2.6 Liao and Zhao test section schematic [31].

While previous investigations on mix convection for large tubes had concluded that heat transfer is always enhanced for downward flow, Liao and Zhao [31] indicate that for miniature tubes the heat transfer coefficient decreases significantly around the pseudocritical region for buoyancy-opposed flow under heating conditions. Additionally, heat transfer enhancement was observed for horizontal and upward flow. They conclude that the Nusselt number decreases with decreasing tube diameter, and they use the Grashof number to create new correlations for miniature tubes that can be used for the design of compact heat exchangers [31].

More recently Liu et al. [32] conducted an experiment to study the heat transfer and pressure drop characteristics of supercritical CO<sub>2</sub> for large diameter tubes. The dependence of Nusselt number on tube diameter, results in the conventional heat transfer correlations for small tubes breaking down when the heat exchanger's tube diameter increases. Thus, Liu et al. experiment features test tubes with ID of 4, 6, and 10.7 mm, positioned horizontally [32], with pressures and temperatures ranging between 7.5 to 8.5 MPa and 298.2 to 340.2 K respectively. Their experiment comprises mass flows between 0.4 and 0.8 kg/s for the CO<sub>2</sub>. Their flow loop set up shown in Figure 2.7 displays four main loops: trans-critical CO<sub>2</sub> heat pump loop; test section loop; cooling water loops; and air loops. The CO<sub>2</sub> is divided into two branches. The trans-critical CO<sub>2</sub> branch incorporates a gas cooler and an internal heat exchanger which allow to improve the efficiency of the expansion valve and the compressor. The evaporator prepares the CO<sub>2</sub> to go into the liquid receiver which holds the CO<sub>2</sub> and ensures that it is entering the compressor. The main goal of the trans-critical CO<sub>2</sub> heat pump cycle is to regulate the CO<sub>2</sub> mass flow rate, pressure, and temperature before entering the test section loop. The test section loop has two sub-coolers that bring the CO<sub>2</sub> temperature down before and after the test section, while a second expansion valve after the second sub-cooler regulates the mass flux of sCO<sub>2</sub> through the test section.

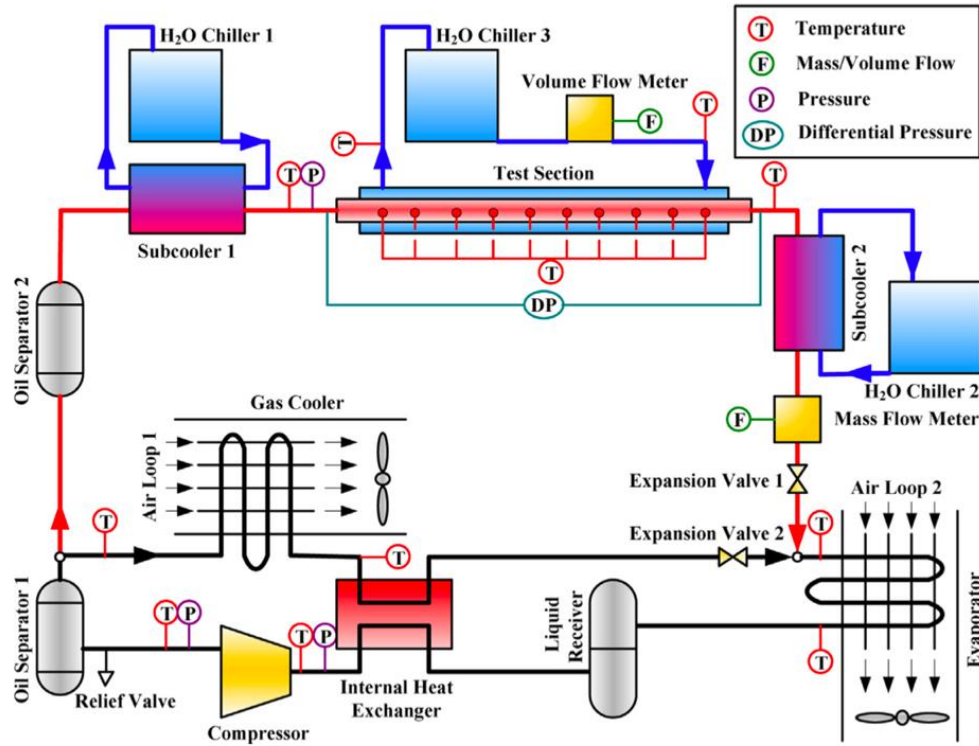


Figure 2.7 Liu et al. flow loop schematic [32].

The test section can be seen in Figure 2.8. It is designed as a 1.3 m long horizontal tube-in-tube heat exchanger, where the CO<sub>2</sub> flows through the inner tube and it is cooled down by the water flowing through the annular passage. Both tubes are made of copper; however, the outer one is covered by a 50mm thick insulating pipe. In order to measure the inlet and outlet test section temperatures for the CO<sub>2</sub> and water sides, K-type thermocouple probes were directly immersed into the fluid. On the other hand, the outer wall temperature of the inner copper tube is measured at 10 equally spaced locations using T-type thermocouples soldered onto the middle side of this wall. The inner wall temperature can be calculated using one-dimensional heat conduction equations. The thermocouples were calibrated to a precision of  $\pm 0.1^\circ\text{C}$ . The inlet pressure is measured by a pressure transducer with an uncertainty of  $\pm 0.075\%$  FS, while the pressure drop is

quantified by a differential pressure transducer with  $\pm 0.075\%$  FS. The CO<sub>2</sub> mass flow rate that enters the test section is measured using a micro motion mass flow meter with a  $\pm 0.044\%$  FS accuracy, while the water mass flow rate is measured by an electromagnetic flow meter with a  $\pm 0.1\%$  FS uncertainty.

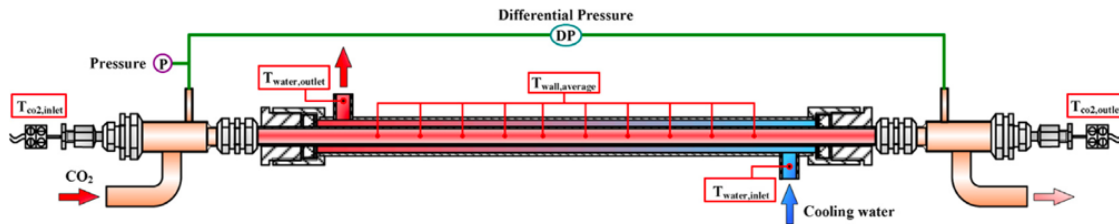


Figure 2.8 Liu et al. test section schematic [32].

Liu et al. [32] concluded that higher mass flow rates enhance heat transfer performance due to an increase in turbulent diffusion; however, higher mass flow rates also result in pressure drops. Additionally, the effective heat transfer of the sCO<sub>2</sub> was substantially affected by tube diameter, with heightened heat transfer coefficients corresponding to larger diameters. Obvious deviations between the experimental data and previously used correlations for small diameter tubes were observed. Thus, more accurate correlations were formulated for the 10.7 mm tubes using a modified Dittus-Boelter correlation based on the data collected during the experiment. The maximum error between the experimental data and the new correlation was found to be  $\pm 15\%$ .

In recent years, new and more complex experimental set ups appear, as Zhang et al. [4] experimentally tested sCO<sub>2</sub> in tubes with inner diameters varying from 4 mm to 10 mm, pressures between 8 MPa and 9 MPa, and mass fluxes from  $160 \text{ kg/m}^2\text{s}$  to  $320 \text{ kg/m}^2\text{s}$ . Their test loop comprises a test section, a refrigeration loop, a cooling water flow loop, a sub-cooling loop, and a preheater; as shown in Figure 2.9. The refrigeration loop cools the CO<sub>2</sub> down to liquid state before

entering a variable speed gear pump which raises the pressure to the desired testing conditions, between 8 and 10 MPa. In order to accurately measure the CO<sub>2</sub> flow rate, the liquid-like fluid enters a buffer chamber under high pressure before running through the mass flux meter. On their experiment, the test section inlet temperature of the sCO<sub>2</sub> is regulated using a *PID* controller, a cast aluminum heater, and a helical coil tube. After the test section, the CO<sub>2</sub> is further cooled by the sub-cooler, before entering the receiver and starting the flow cycle again. The test section consists of a 316 stainless-steel horizontal counter-flow tube-in-tube heat exchanger with a length of 1,000 mm. The inlet and outlet temperatures for water and CO<sub>2</sub> are measured by 4 K-type thermocouples directly immersed inside of the fluid, while 3 additional K-type thermocouples measure the outside wall temperature of the inner tube at the middle point of the test section. They are arranged at the 4, 8, and 12 o'clock positions, as pictured in Figure 2.10.

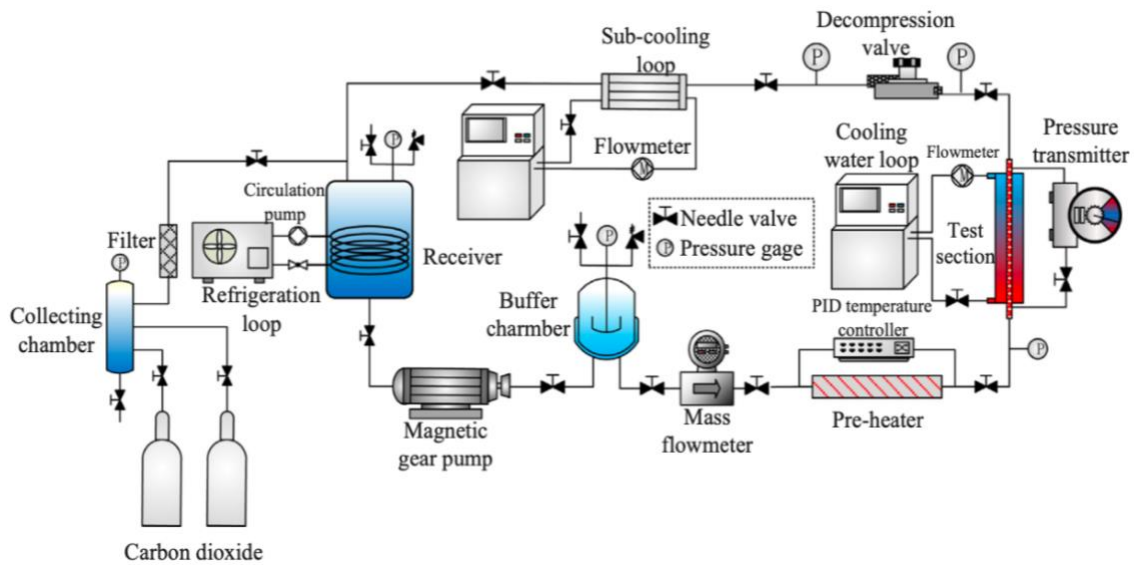


Figure 2.9 Zhang et al. flow loop schematic [4].

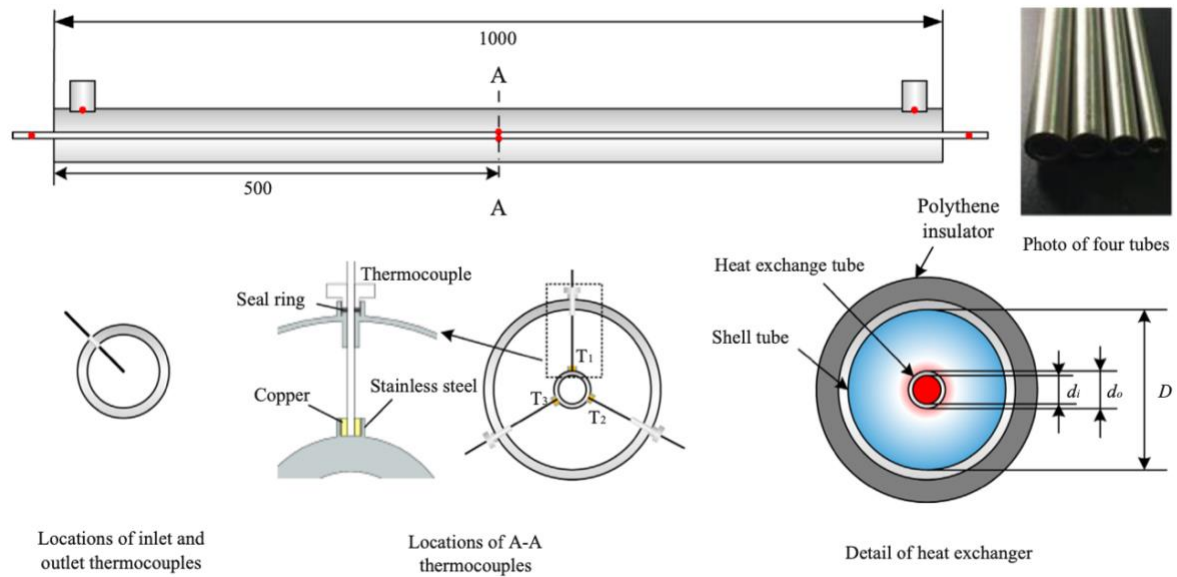


Figure 2.10 Zhang et al. test section schematic [4].

All thermocouples were calibrated to an accuracy of  $\pm 0.1^\circ\text{C}$ . The flow rate of the cooling water jacket is regulated using a centrifugal pump and measured by a turbine flow meter with a  $\pm 1\%$  accuracy, while its temperature is controlled by a thermostat. The pressure drop across the test section is measured using pressure transmitters installed at the inlet and outlet with a  $\pm 1$  Pa uncertainty; on the other hand, pressure gauges measure the pressure at different critical locations in the flow loop with an accuracy of  $\pm 2\%$  as indicated in Figure 2.9. After all the uncertainties are taken into consideration, the range of uncertainty for heat transfer coefficients in Zhang et al. [4] experiment was found to be between 3.55% and 15.73%.

Tests were conducted for tubes with different diameters under different pressures and mass fluxes. The inlet and outlet temperature of the fluids, the outer wall temperature, the flow rate of the cooling water, and the pressure drop across the test section were documented under steady state conditions. Their experimental results are compared to previous heat transfer correlations for  $\text{CO}_2$ , resulting in relatively large deviations. It was found that these correlations fail to predict the heat

transfer behavior of CO<sub>2</sub> accurately when the experimental conditions differ from the ones used to formulate the correlations. Thus, Zhang et al. [4] stress the importance of formulating new correlations that can be used to predict heat transfer coefficients under different working conditions for tubes with different diameters, by accounting for the natural convection inside the tubes. Thus, the effects of buoyancy and inner diameter on heat transfer are introduced into their correlations, resulting in an absolute average deviation of 13.06%.

For the case of sCO<sub>2</sub> flow in horizontal tubes, most of the recent simulations are validated using the experimental results of Dang and Hihara [21]. Dang and Hihara conducted a series of experiments featuring a horizontal tube in tube counterflow heat exchanger with inner copper tubes with IDs of 1 mm, 2 mm, 4 mm, and 6 mm and length of 500 mm [21]. Their experiment uses a constant heat flux boundary condition created by a cooling water jacket inside of an acrylic tube. Their experiment was performed for heat fluxes ranging from 6  $kW/m^2$  to 33  $kW/m^2$  and mass fluxes  $G = 200, 400, 600, \text{ and } 800 \text{ kg}/m^2s$ .

Their loop consists of a charging port, a gear pump, a mass flow meter, a pressure relief valve, an internal heat exchanger, a heater, a test section with its corresponding cooling water loop, and a sub-cooler. The corresponding loop schematic is shown in Figure 2.11. The CO<sub>2</sub> enters the closed flow loop using a plunger pump. A magnetic gear pump with an inverter is used to run the CO<sub>2</sub> at the desired flow rate. Aft the pump, the internal heat exchanger and the preheater heat the CO<sub>2</sub> up in order to achieve the desired experimental temperatures for the test section, ranging between 30°C and 70°C. When the CO<sub>2</sub> comes out of the test section, it is cooled down by the internal heat exchanger and the sub-cooler in order to turn into a more liquid-like state with a higher viscosity and density to improve the performance of the gear pump.

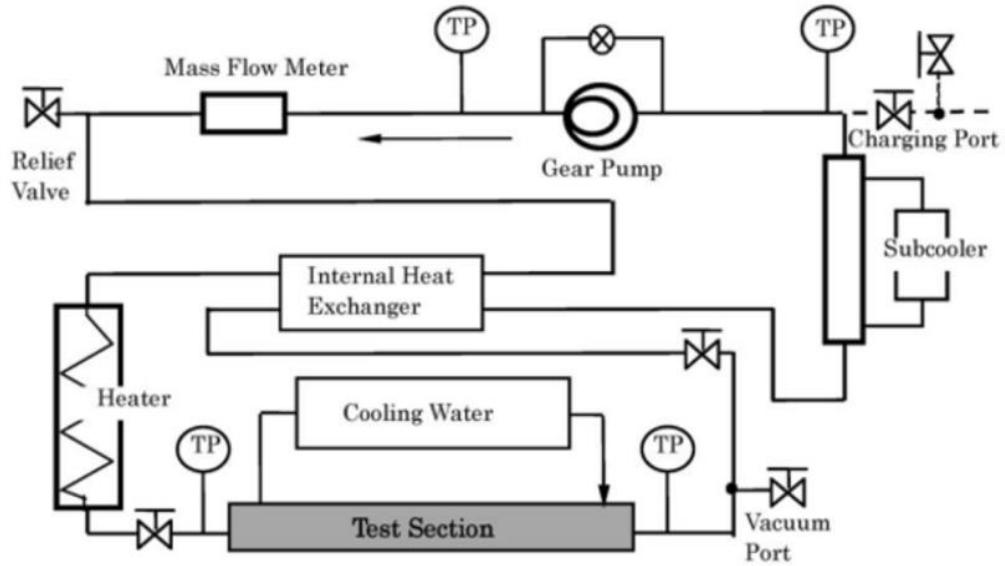


Figure 2.11 Dang and Hihara flow loop schematic [21].

As previously mentioned, the test section consists of a 500 mm horizontal tube-in-tube counterflow heat exchanger. The inner tube is made of smooth cooper, containing the sCO<sub>2</sub> while the water flows through the outer annular passage contained by an acrylic resin tube. The inner diameters for the different testing copper tubes were 1, 2, 4, and 6 mm, all of them with a wall thickness of 1 mm. The corresponding annular gaps for the inner tube IDs were 1.5, 2, 2, and 3 mm, respectively [21]. The test section was wrapped in polystyrene insulation with a thickness of 25 mm in order to reduce heat loss to the environment. The inlet and outlet temperature for the CO<sub>2</sub> was measured using T-type thermocouples, while the inlet and outlet temperature for the water was measured with Pt100 sensors with an accuracy of  $\pm 0.03^{\circ}\text{C}$ . Additionally, the outer wall temperature of the copper was measured at 10 equally spaced locations along the tube using T-type fine thermocouples. The location of these thermocouples can be seen on the schematic of the test section on Figure 2.12. All thermocouples were calibrated to an accuracy of  $\pm 0.1^{\circ}\text{C}$ . The inlet and outlet pressure of the CO<sub>2</sub> was measured using pressure transducers with an accuracy of

$\pm 0.001$  MPa. The Coriolis mass flow meter used on their experiment has an accuracy of  $\pm 0.1\%$  FS while the mass flow rate for the water loop was measured with an accuracy of  $\pm 0.5\%$  FS.

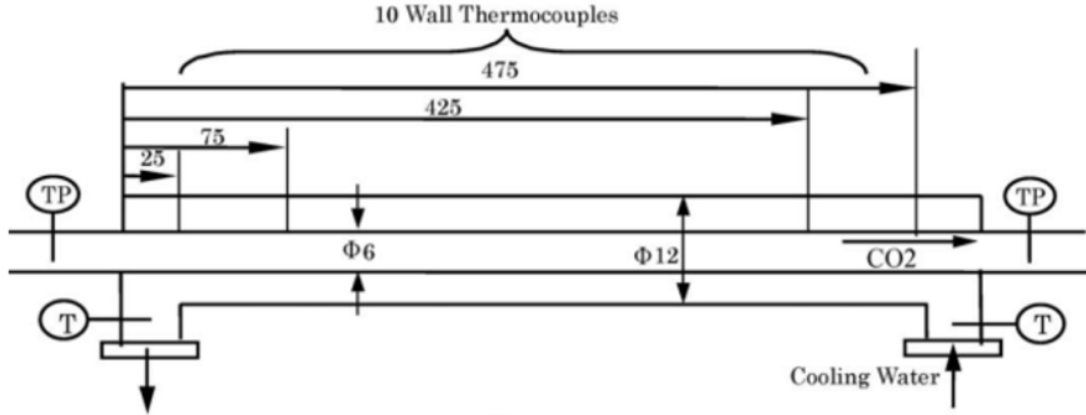


Figure 2.12 Dang and Hihara test section schematic [21].

A new modified Gnielinski correlation (Eq. 2.1) is formulated by using the pseudocritical temperature ( $T_{pc}$ ) as a reference and introducing an “integrated” specific heat ( $\bar{c}_p$ ) value in the calculations. The expression is based on the average wall, bulk, and film temperatures in the test section. The friction factor is calculated using the Filonenko [33] correlation shown in Eq. 2.2 and evaluated using film properties [34].

$$Nu = \frac{(f_f/8)(Re_b - 1000)Pr}{1.07 + 12.7\sqrt{f_f/8}(Pr^{2/3} - 1)} \quad (2.1)$$

$$f = [1.82 \log_{10}(Re_b) - 1.64]^{-2} \quad (2.2)$$

where the subscripts  $b$  and  $f$  refer to quantities evaluated at bulk and film temperatures, respectively. The film temperature is calculated as:

$$T_f = \frac{T_b + T_w}{2} \quad (2.3)$$

with  $T_w$  being the inner wall temperature.

The main modification from the original Gnielinski correlation comes in the calculation of the Prandtl number, which changes based on the quantities taken at bulk and film conditions (Eq. 2.4).

$$Pr = \begin{cases} \frac{c_{p,b}\mu_b}{k_b} & \text{for } c_{p,b} \geq \bar{c}_p \\ \frac{\bar{c}_p\mu_b}{k_b} & \text{for } c_{p,b} < \bar{c}_p \text{ and } \frac{\mu_b}{k_b} \geq \frac{\mu_f}{k_f} \\ \frac{\bar{c}_p\mu_f}{k_f} & \text{for } c_{p,b} < \bar{c}_p \text{ and } \frac{\mu_b}{k_b} < \frac{\mu_f}{k_f} \end{cases} \quad (2.4)$$

where the “integrated” specific heat capacity ( $\bar{c}_p$ ) is calculated using the fluid enthalpies ( $s$ ) at bulk and wall conditions as shown in Eq. 2.5.

$$\bar{c}_p = \frac{(s_b - s_w)}{(T_b - T_w)} \quad (2.5)$$

The heat transfer coefficient can finally be calculated using the thermal conductivity of the CO<sub>2</sub> at film temperature ( $k_f$ ):

$$h = \frac{Nuk_f}{D_h} \quad (2.6)$$

Their correlation proved to be accurate within 20% of their experimental data.

## 2.4 Summary

From the previous experimental and numerical work presented on the previous sections, ERAU has developed and deployed an sCO<sub>2</sub> flow loop, with the goal of this thesis being documenting the benchmarking efforts. The flow loop test section consists of a horizontal tube-in-tube counterflow heat exchanger with a circular cross section, where all the experimental measurements are carried out. The effects of mass flux, pressure, and heat flux on heat transfer performance are studied and compared against previous work from the literature for the purpose of validation. The goal of the current work is to benchmark and validate the designed flow loop against the work from Dang and Hihara [21].

### **3 Methodology**

The methodology chapter of this thesis outlines the systematic approach employed to investigate the heat transfer capabilities of sCO<sub>2</sub> through experimental testing utilizing the dedicated flow loop. This chapter provides a comprehensive overview of the strategies and procedures undertaken to address the research objectives pertaining the characterization and benchmarking of the sCO<sub>2</sub> flow loop used in this study. The methodology encompasses a series of carefully designed experimental procedures to measure key parameters such as heat transfer coefficients, pressure drops, and temperature distributions across different components of the flow loop. Central to the experimental setup is the utilization of specialized instrumentation and analytical tools to accurately predict and capture the intricate heat transfer processes occurring within the sCO<sub>2</sub> flow. High-resolution sensors and careful data reduction procedures are employed to facilitate detailed analysis of heat transfer phenomena under varying flow rates, temperatures, and pressures. Through the comprehensive methodology outlined in this chapter, this research endeavors to advance the understanding of sCO<sub>2</sub> heat transfer behavior and contribute valuable insights to the development of heat transfer research capabilities for sCO<sub>2</sub> at ERAU's Thermal Science Lab.

#### **3.1 Experimental Apparatus**

The flow loop consists of the following major components which can be seen in Figure 3.1: test section, constant temperature bath, accumulator, gear pump, Coriolis mass flow meter, and pre-heater. It has the capability to run sCO<sub>2</sub> experiments up to 1,500 psi (10.34 MPa) and 85°C (353.15 K).

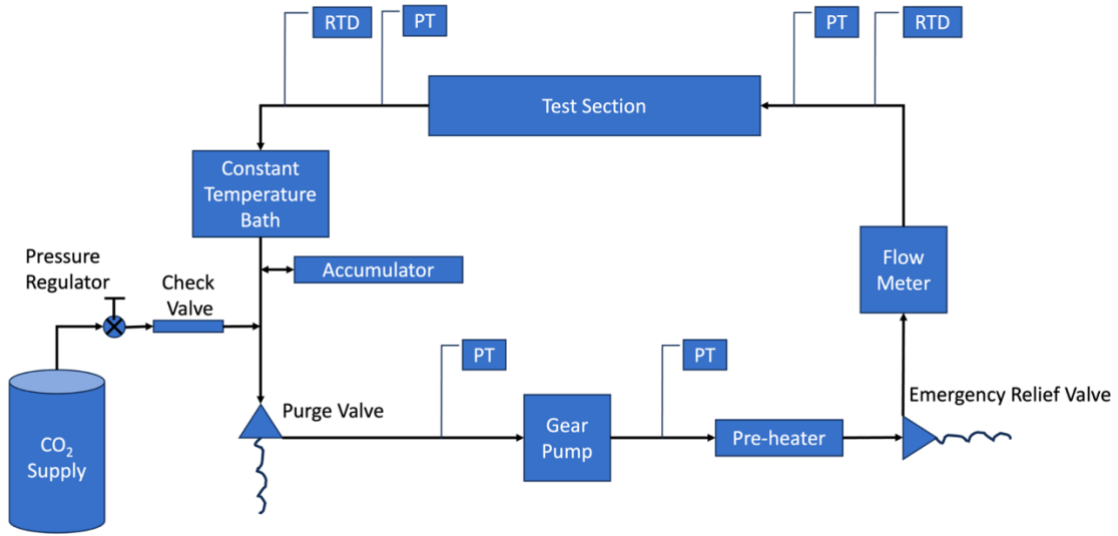
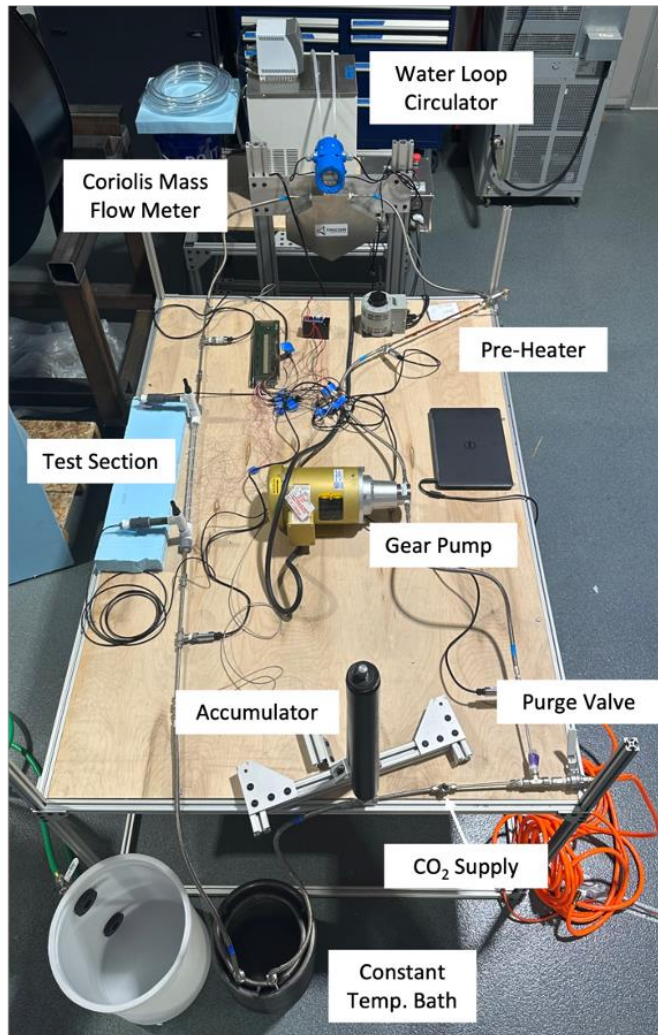


Figure 3.1 Flow loop schematic.

The sCO<sub>2</sub> exiting the test section first passes through a constant temperature bath to bring the bulk temperature of the fluid down, yielding a more viscous, liquid-like fluid. This was done to increase the efficiency of the gear pump. The heat exchanger was designed to be infinitely long so that the bath temperature, which was controlled by a 7 kW chiller (JHI-2000-M), could be set to the same desired temperature of the sCO<sub>2</sub>. The flow then passes through the magnetically driven gear pump (GC-M23.PDS.E-N2CH30) and Coriolis mass flow meter (TCM-1550-FK-SGSS-CSDS). A gear pump was selected due to its low leakage, and self-priming ability, and smooth flow output. A Coriolis mass flow meter was chosen because with a compressible flow, the density variations throughout the loop would cause issues with a volumetric flow rate reading, so a true mass flow rate reading was needed. Coriolis mass flow meters also have a very low pressure drop across the system, which prevents any sharp pressure gradients from developing. This is especially important due to the thermophysical properties of sCO<sub>2</sub> having a high pressure dependency and vary greatly around the critical point. The accuracy of the flow meter is  $\pm 0.3\%$ . Leaving the flow



*Figure 3.2 Flow loop experimental setup.*

meter, the flow then passes through a pre-heater which reintroduces the heat lost in the test section and constant temperature bath and sets the inlet temperature of the test section. The pre-heater consists of a Nichrome heating wire wrapped around a copper tube, and when a voltage is applied, the resistance of the wire heats the copper which in turn heats the sCO<sub>2</sub>. Due to power consumption limitations in the lab, only 1.4 kW of heat could be added back into the system with the variac operating at 140 Volts and 10 Amps. The loop is charged from a 2,000 psi storage tank controlled by a pressure regulator and has a ball valve with a line to the fume hood to purge the

system after operation. A Nitrogen charged accumulator was incorporated into the loop to dampen out any pressure changes, and to keep the loop at constant pressure with small temperature variations and bleed off. All tubing is covered by 0.5 in. rubber foam insulation, in order to diminish heat loss to the environment. Figure 3.2 shows the actual flow loop deployed without insulation for easier visualization of all the main components.

### **3.1.1 Test Section Design**

The test section is a horizontal tube-in-tube counterflow heat exchanger comprising a copper inner tube with ID of 6 mm and thickness of 1 mm and an acrylic outer tube with ID of 12.7 mm and thickness of 3.175 mm. The sCO<sub>2</sub> flows inside of the copper tube while the cooling water flows through the annular passage. The total length of the test section is 500 mm, and it is covered by fiberglass insulation. A 400 mm adiabatic section is added before the inlet of the test section to allow for sufficient flow development. The bulk flow temperature is measured at the inlet and outlet of the test section using Class A RTDs, with an accuracy of  $\pm 0.25^\circ\text{C}$ . Additionally, 20 T-type 36-gauge thermocouples are used to measure the wall temperature at 10 equally spaced axial locations, as shown in Figure 3.3. The first and last set of thermocouples are positioned 25 mm away from the entrance and exit of the test section respectively, while the rest have a spacing of 50 mm in between them. As seen in Figure 3.4, each location has two thermocouples attached to the outside copper wall at the 3 and 9 o'clock positions. One dimensional heat conduction equation and copper properties are used to calculate the inside wall temperature. After calibration, the thermocouples provide local wall temperature measurements with an accuracy of  $\pm 0.1^\circ\text{C}$ . Pressure measurements are taken using pressure transducers with an accuracy of 0.25% at the inlet and outlet to calculate the pressure drop across the test section. For the water loop, a 1 kW cooling circulator controls the water mass flow and inlet temperature, while ultra-precise RTDs are used

to calculate the temperature of the water entering and exiting the test section with an accuracy of  $\pm 0.03^\circ\text{C}$ . Lastly, an analog flow meter with a 2% accuracy indicates the mass flow of the water jacket in the test section.

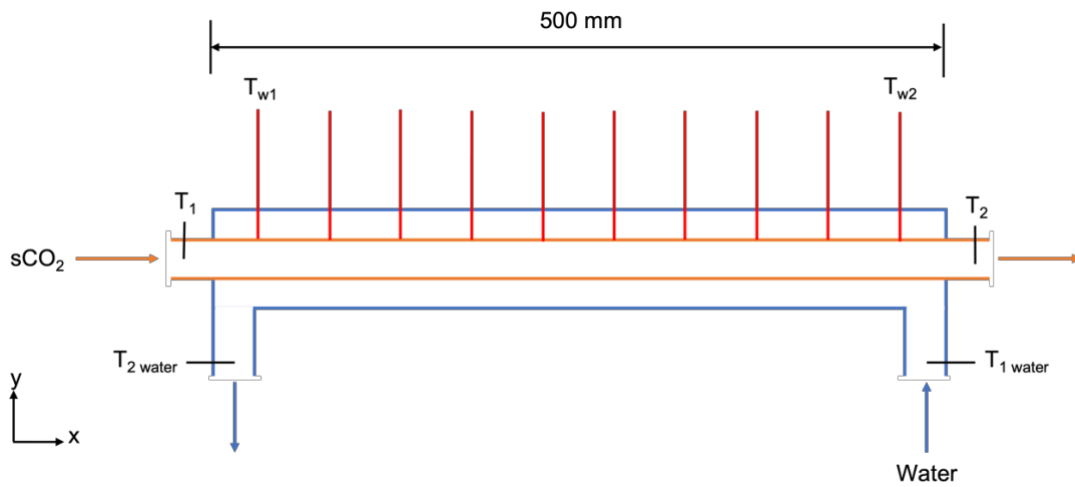


Figure 3.3 Schematic of test section.

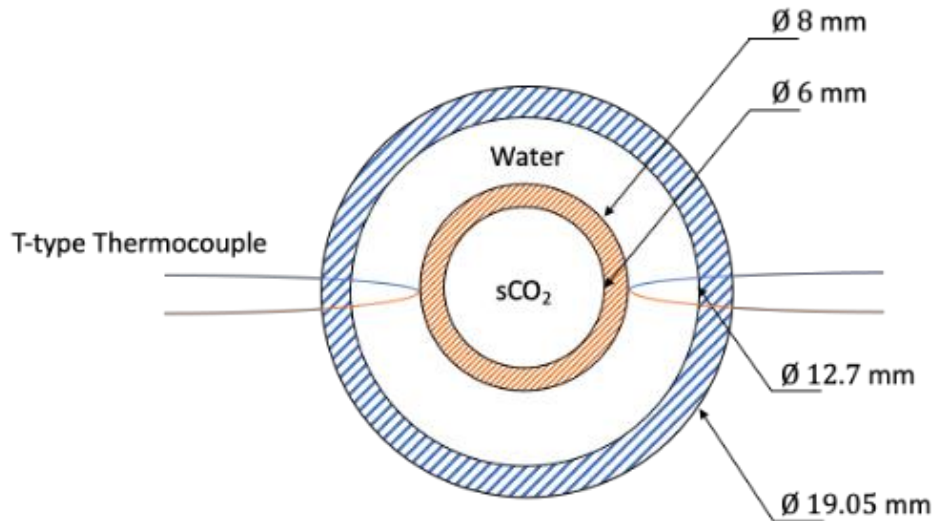
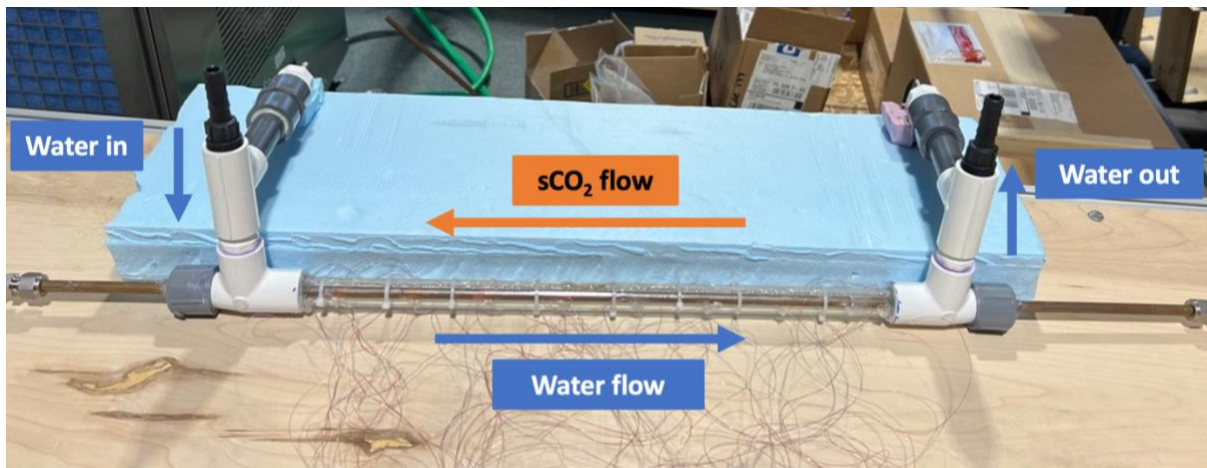


Figure 3.4 Test section cross section.

The current test section design can be observed in Figure 3.5, where the fiberglass insulation has been removed for easier visualization. The counterflow heat exchanger nature of the test section is also indicated, where the sCO<sub>2</sub> and water flow in opposite directions. The thermal entrance length of the test section is 400 mm, while the hydrodynamic entrance length is 200 mm, following the study from Chao et al. [24].



*Figure 3.5 Experimental test section.*

Additionally, the test section was modeled in CAD in order to allow for supplemental CFD simulations that will be conducted using the model shown in Figure 3.6. All materials and essential dimensions are true to the physical model, except for the length of the copper tube. Compared to the physical test section, the copper tube for the CFD model will be extended in both directions to allow for sufficient sCO<sub>2</sub> hydraulic development prior to entering the test section and to prevent potential backflow from the outlet.

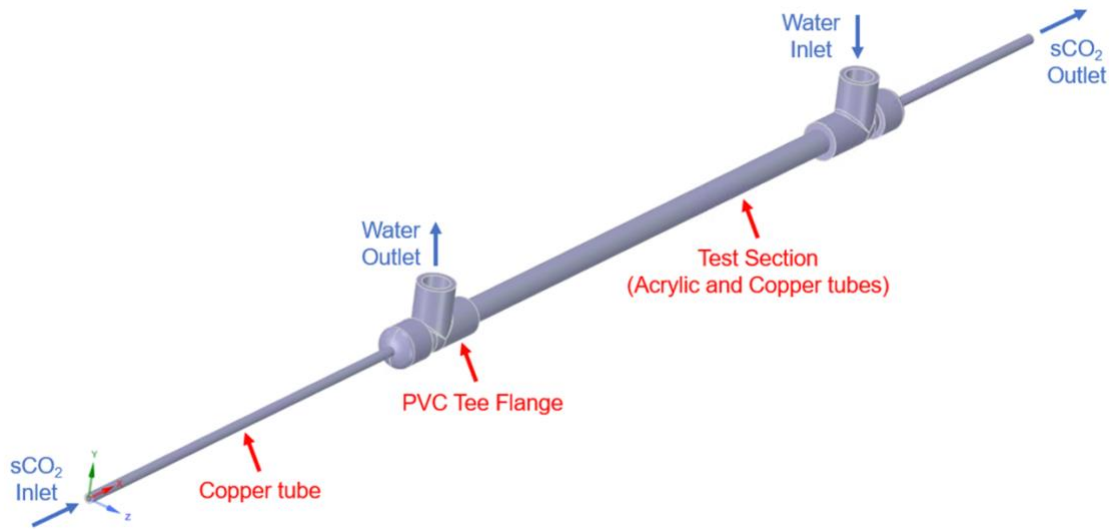


*Figure 3.6 Simplified test section model for CFD.*

### **3.1.2 Pre-heater and Cooler Modification**

The last version of the deployed flow loop introduces a few design modifications when compared to the previously described layout. This version was used for the last set of supercritical tests. The preheater has been substituted by a stainless-steel coil submerged in a water tank with an immersive heater inside. The immersive heater is connected to a variac variable transformer which allows to manually regulate the output voltage going into the immersive heater; consequently, allowing to adjust the water temperature. The length of the coil is 21 m considered to be infinitely long; thus, the water temperature will equal the CO<sub>2</sub> temperature coming out of the component. Since the coil was moved from the cooler to the pre-heater section of the flow loop, there is currently no cooling system after the test section. Since the CO<sub>2</sub> cannot be cooled down further after the test section, the  $q$  added to the system in the pre-heater must be the same as the  $q$  removed in the test section in order to attain thermal balance; limiting the range of temperatures and heat fluxes at which testing can be conducted.

### **3.1.3 Safety Features**

Due to the nature of the test conducted, different safety precautions were taken when designing and operating the flow loop. First, the high testing pressures (8 to 10MPa) could cause overload failure due to overpressurization. In order to tackle this issue, a pressure relief valve was added to the rig. The valve will open and release CO<sub>2</sub> if pressures above 1,500 psi are reached, corresponding to the maximum pressure rating for the pump. All other components are rated for higher pressures. Another concern is the fatigue failure that could occur from the cyclical pressurization and depressurization of the rig. Thus, the loop is loaded and unloaded at a rate around 80 psi/min as to not shock the system [35]. Also, at high pressures, CO<sub>2</sub> might react with water vapor if residual air is trapped inside of the rig when the loop is not operating, creating carbonic acid and potential corrosion failure. In order to get rid of this possibility, the loop is purged before every test by flushing pressurized CO<sub>2</sub> before beginning to load the system. Lastly, asphyxiation when purging the system had to be considered. To prevent this from happening, a hose connects the purge valve to the fume hood, keeping the loop operators away from the CO<sub>2</sub> coming out of the system during depressurization [35].

### **3.2 Data Collection**

The experimental data was recorded by a Keysight data acquisition system (DAQ). Steady state was considered to be achieved when all instrumentation had a standard deviation was equal or less than the instruments accuracy when averaged over time [35]. Data was collected at a rate of 0.2 Hz and averaged over a ten-minute period. For the flow meter data, the Coriolis mass flow meter recorded the values using its own software, so the DAQ was not needed. In this case, the mass flow values were recorded at a rate of 2.0 Hz and again averaged over a ten-minute period. The averaged values from the DAQ and Coriolis mass flow meter were then used for the data reduction procedure.

A few conversions needed to be done for the instrumentation. The pressure transducers measured voltage that needed to be converted to pressure values. In order to do so a linear fit was assumed with the formula shown on Eq. 3.1. Where  $P$  is the calculated pressure,  $V$  is the measured voltage,  $a$  the slope, and  $b$  is the offset. The constant  $a$  is calculated by dividing the FS of the pressure transducer (2,000 psi) by the FS of the voltage output (10 V). The offset  $b$  is calculated by measuring the pressure readings when there is no pressure in the loop for 1 minute. These values are averaged and used to “zero out” the pressure transducer [35].

$$P = a \cdot V + b \quad (3.1)$$

For the temperature readings, it was necessary to convert the resistance output recorded by the 3 wire RTDs to temperature using Eq.3.2.

$$T = \frac{\left(\frac{\Omega_1 - \Omega_2}{100}\right) - 1}{\alpha} \quad (3.2)$$

where  $\alpha = 0.00385 \Omega / \Omega / ^\circ\text{C}$ ,  $\Omega_1$  is the resistance recorded by the RTD, and  $\Omega_2$  is the resistance recorded by the ground line. All other instrumentation readings were recorded in the intended units and did not require any calibration or conversion.

### 3.3 Data Reduction

The experimental parameters measured were temperature ( $T$ ) and pressure ( $P$ ) at the inlet and outlet of the test section. Mass flow ( $\dot{m}$ ) for the water and  $\text{CO}_2$  were also measured through an analog flowmeter and a Coriolis mass flow meter respectively. Heat flux ( $q_w''$ ) through the 6 mm ID test section was then calculated. The total amount of heat transferred was analyzed by performing energy balance on the water side or the  $\text{CO}_2$  side and corresponds to:

$$q_w = q_{H_2O} = q_{CO_2} = \dot{m}_{H_2O} c_p \Delta T_{H_2O} = \dot{m}_{CO_2} \Delta S_{H_2O} \quad (3.3)$$

It was found that using energy balance for the  $\text{CO}_2$  side to calculate the total amount of heat transferred was more accurate due to the small  $\Delta T$  on the water side and the RTD uncertainty.

Thus, the CO<sub>2</sub> enthalpy ( $s$ ) at the inlet and outlet of the test section is obtained from REFPROP [36] by using the CO<sub>2</sub> bulk temperature and pressure readings at these two locations, allowing for the calculation of  $\Delta s$ . The heat flux can then be calculated using the total inner surface area of the copper pipe ( $A_{inner}$ ):

$$q_w'' = \frac{q_w}{A_{inner}} \quad (3.3)$$

The average heat transfer coefficient ( $\bar{h}$ ) is calculated from the logarithmic mean temperature difference between CO<sub>2</sub> and inner wall temperatures (Eq.3.4 and Eq. 3.5).

$$LMTD_w = \frac{(T_{CO_2} - T_w)_1 - (T_{CO_2} - T_w)_2}{\ln\left(\frac{(T_{CO_2} - T_w)_1}{(T_{CO_2} - T_w)_2}\right)} \quad (3.4)$$

$$\bar{h} = \frac{q_w''}{LMTD_w} \quad (3.5)$$

where subscripts 1 and 2 represent the inlet and outlet conditions with  $T_{CO_2}$  corresponding to the CO<sub>2</sub> temperatures measured by the inlet and outlet RTDs and  $T_w$  being the inner wall temperatures. The inside wall temperatures ( $T_w$ ) can be obtained from one-dimensional heat conduction equations and the thermocouple readings for the outer wall, as shown on Eq. 3.6.

$$T_{w,inner} = q_w \frac{\ln\left(\frac{r_{outer}}{r_{inner}}\right)}{2\pi L_i k} + T_{w,outer} \quad (3.6)$$

where  $k$  is the thermal conductivity of the copper pipe and  $L$  is the total length of the test section.

Following the experiment from Dang and Hihara [21], the test section inlet temperature was varied from 30°C to 70°C, and the average heat transfer coefficient is compared against the average of the inlet and outlet bulk temperatures Eq. 3.7 [21].

$$\bar{T}_b = \frac{T_{CO_21} + T_{CO_22}}{2} \quad (3.7)$$

Additionally, with the proposed experimental set up, it is possible to calculate the local heat transfer coefficient ( $h$ ) at the different thermocouple locations. To calculate the local heat transfer coefficient, the test section is divided into 10 subsections corresponding to the thermocouple locations. The total amount of heat transferred at each subsection is calculated using Eq. 3.8.

$$q_{subsection} = q_w'' A_{subsection} \quad (3.8)$$

where  $A_{subsection}$  is the inner area of the copper pipe for each subsection.

From the thermocouple readings, the inner wall temperature ( $T_w$ ) is calculated following Eq. 3.6. With the inner wall temperatures, the bulk temperature at each of the thermocouple locations is estimated using Eq. 3.9.

$$T_b = T_{w,inner} + \frac{q_{subsection}}{\dot{m}c_p} \quad (3.9)$$

Once bulk and wall temperatures are known, the local heat transfer is calculated as:

$$h = \frac{q_{subsection}}{A_{subsection}(T_w - T_b)} \quad (3.10)$$

The previous method is an estimation, since  $h$  and  $c_p$  are assumed constant for each subsection. However, it is the method used by Dang and Hihara [21] on their experiment and it was followed for this study. Future test section designs will incorporate instrumentation that allows to measure local heat transfer in a more accurate way.

### 3.4 Uncertainty Analysis

In order to calculate the maximum uncertainty for average heat transfer coefficient ( $\bar{h}$ ) and total amount of heat transferred ( $q$ ), it is important to account for the uncertainty of all the instrumentation used in the experimental set up. Table 3.1 summarizes the instrumentation used as well as its corresponding accuracy. All accuracy values correspond to percentage of the reading, unless full scale (FS) is specified.

Table 3.1 Instrumentation accuracy.

Measurement	Instrumentation	Accuracy
$\dot{m}_{CO_2}$	Coriolis Mass Flow Meter	$\pm 0.1\%$ for liquids $\pm 0.5\%$ for gases
$\dot{m}_{H_2O}$	Analog Mass Flow Meter	$\pm 2\%$ (FS)
$T_b$	Class A RTD (3 wire RTD)	$\pm 0.25\text{ }^\circ\text{C}$
$T_w$	T-Type 36-gauge thermocouples	$\pm 0.1\text{ }^\circ\text{C}$
$T_{H_2O}$	Ultra-precise RTD (4 wire RTD)	$\pm 0.03\text{ }^\circ\text{C}$
$P$	Pressure Transducer	$\pm 0.25\%$

To calculate the uncertainty in  $\Delta T_{H_2O}$  and  $\Delta T_{CO_2}$ , Eq. 3.11 and Eq. 3.12 are used respectively, where  $\delta T_{H_2O}$  and  $\delta T_{CO_2}$  are the different RTD uncertainties for water and CO<sub>2</sub>, and subscripts 1 and 2 represent inlet and outlet conditions.

$$\delta \Delta T_{H_2O} = \sqrt{(\delta T_{H_2O})_1^2 + (\delta T_{H_2O})_2^2} = \sqrt{2} \cdot \delta T_{H_2O} \quad (3.11)$$

$$\Delta T_{CO_2} = \sqrt{(\delta T_{CO_2})_1^2 + (\delta T_{CO_2})_2^2} = \sqrt{2} \cdot \delta T_{CO_2} \quad (3.12)$$

In a similar fashion, the uncertainty in heat ( $q$ ) and average heat transfer coefficient ( $\bar{h}$ ) can be calculated using  $\Delta T_{H_2O}$  and  $\delta \Delta T_{CO_2}$  on Eq. 3.13 and Eq. 3.14.

$$\delta q = \sqrt{\left(\frac{\delta T_{H_2O}}{\Delta T_{H_2O}}\right)^2 + \left(\frac{\delta \dot{m}_{H_2O}}{\dot{m}_{H_2O}}\right)^2} \quad (3.13)$$

$$\delta \bar{h} = \sqrt{\left(\frac{\delta q}{q}\right)^2 + \left(\frac{\delta LMTD_w}{LMTD_w}\right)^2} \quad (3.14)$$

Following the previous equations, the maximum uncertainty in heat ( $q$ ) was calculated to be  $\pm 8.78\%$  while the maximum uncertainty in average heat transfer coefficient ( $\bar{h}$ ) is  $\pm 8.83\%$  [35].

### 3.5 Pretest Prediction Code

Along with the experimental set up, a 1-D analysis code was created to analyze the flow properties at different critical locations throughout the loop. The analysis code is used to set up the operating conditions for the different controls in the flow loop, reducing the time that it takes to obtain the desired temperatures and pressures in the test section. Additionally, it assures that all the components in the loop are operating in safe conditions and inside their operational pressure range. The flow loop analysis code was built in MATLAB and references REFPROP [36] to obtain the sCO<sub>2</sub> thermophysical property values. In order to do so, REFPROP property tables are exported into Excel and MATLAB reads this file, interpolating the corresponding CO<sub>2</sub> thermophysical properties for a specific temperature and pressure input.

The simulation uses the Darcy-Weisbach equation (Eq. 3.15) to calculate the pressure loss along the whole loop. The friction factor is calculated following Filonenko [33] and Dang and Hihara [21] correlations (Eq. 2.2). On the other hand, in order to predict the pressure loss across the water loop, the Moody friction factor equation is used (Eq. 3.16), and the pressure loss is again calculated using the Darcy-Weisbach equation. The Coriolis flow meter specifications prove that the pressure loss is negligible for this component for our test conditions. Additionally, the accumulator should have no pressure loss as it is considered a “bleed proof system”. Lastly, the pump will have a pressure differential equal to the total pressure loss across the rest of the flow loop.

$$\frac{\Delta P}{L} = f \frac{\rho v^2}{2 D_h} \quad (3.15)$$

$$f = 0.0055 \left[ 1 + \left( 2 \times 10^4 \frac{\epsilon}{D_h} + \frac{10^6}{Re} \right)^{\frac{1}{3}} \right] \quad (3.16)$$

Regarding the temperature calculations, the preheater uses the mean (“integrated”) heat transfer coefficient ( $\bar{h}$ ) between the inlet temperature of the preheater and the desired test section inlet temperature. This mean heat transfer coefficient for the CO<sub>2</sub> is calculated by performing trapezoidal numerical integration on the heat transfer coefficient, analyzed using the Gnielinski correlation (Eq. 2.1) between the inlet and outlet temperature of the component. The temperature difference across this component can be calculated using the heat input set by the power provided to the heating wire ( $q_{preheater}$ ) as shown in Eq. 3.17.

$$\Delta T = \frac{q_{preheater}}{\bar{h}A} \quad (3.17)$$

For the chiller, a similar procedure is followed where the mean heat transfer coefficient across the section is integrated between the inlet temperature and the bath temperature. It is important to notice the area change between the test section (6 mm ID) and the coil used for the chiller (19.05 mm ID), resulting in lower heat transfer values for the sub-cooler. The outlet temperature is calculated by performing energy balance for the CO<sub>2</sub>.

For the test section, the average heat transfer coefficient for the CO<sub>2</sub> was calculated by stepping through the test section and assuming constant  $c_p$  and  $h$  for each subsection, while using the desired constant heat flux ( $q_w''$ ) for the CO<sub>2</sub> energy balance equation (Eq. 3.18). Here, the enthalpy at the outlet of each subsection can be calculated, and the corresponding temperature is read from the REFPROP values. The mean  $h$  for each of the subsections was calculated using Gnielinski correlation (Eq. 2.1) and the numerical integration described previously. The inlet temperature for the water loop is approximated for the first iteration and energy balance for the water side (Eq. 3.19) is performed to obtain the water outlet temperature using the desired heat flux. The actual

heat flux is calculated from the LMTD equation (Eq. 3.20 and Eq. 3.21), and the water inlet temperature is iterated until the calculated heat flux matches the desired one. One-dimensional heat conduction through the copper pipe is ignored for the test section calculations since it is deemed negligible for the purpose of the pre-test prediction tool. The rest of the loop is perfectly insulated and is considered adiabatic.

$$q_w'' A_{subsection} = \dot{m}_{CO_2} \Delta s_{CO_2} \quad (3.18)$$

$$q_w'' A_{subsection} = \dot{m}_{H_2O} c_p \Delta T_{H_2O} \quad (3.19)$$

$$q_{actual}'' = U \left( \frac{(T_{CO_2} - T_{water})_1 - (T_{CO_2} - T_{water})_2}{\ln \left( \frac{(T_{CO_2} - T_{water})_1}{(T_{CO_2} - T_{water})_2} \right)} \right) \quad (3.20)$$

where  $U$  is the overall heat transfer coefficient calculated as:

$$U = \frac{1}{\frac{1}{h_{H_2O}} + \frac{1}{h_{CO_2}}} \quad (3.21)$$

Figure 3.7, Figure 3.8, and Figure 3.9 summarize an example case for the heat transfer coefficient integration and average values used for the cooler, preheater, and test section calculations respectively. Furthermore, Figure 3.9 shows the average heat transfer coefficient used for the local calculations at each of the subsections. The example case corresponds to Run 10 on the test matrix (Table 3.2), and it is further described in the results chapter. This test was run at 8 MPa, with a CO<sub>2</sub> inlet temperature of 50°C (323.15 K) and a mass flux of 200 kg/m<sup>2</sup>s, while assuming a constant heat flux of 33 kW/m<sup>2</sup>.

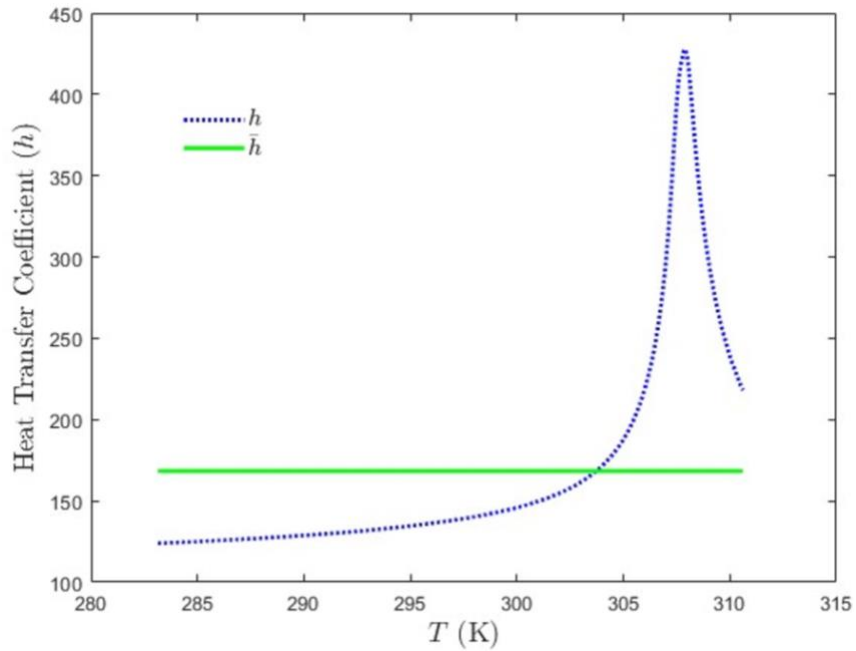


Figure 3.7 Cooler average heat transfer coefficient ( $\bar{h}$ ) and actual heat transfer coefficient for the range of operating temperatures ( $h$ ).

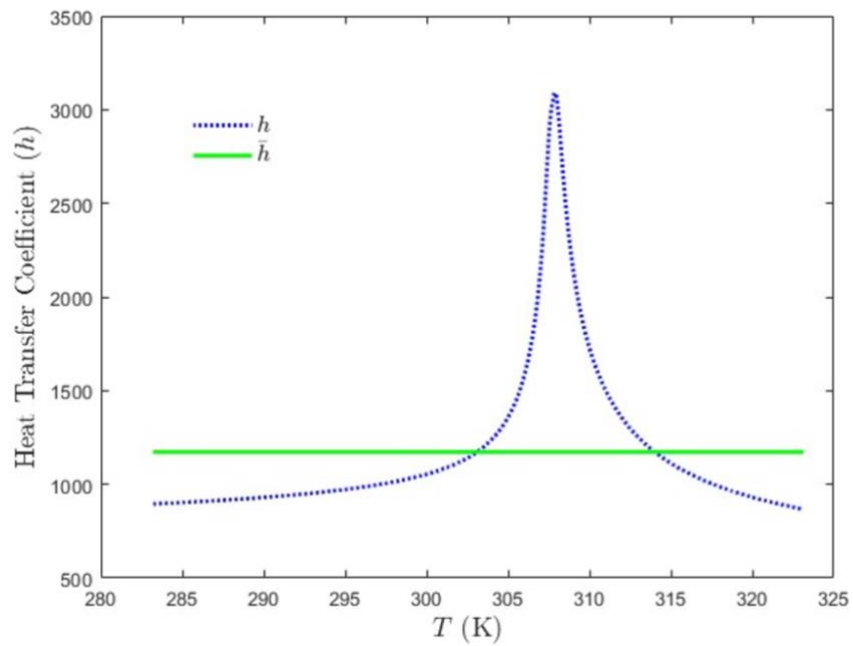


Figure 3.8 Preheater average heat transfer coefficient ( $\bar{h}$ ) and actual heat transfer coefficient for the range of operating temperatures ( $h$ ).

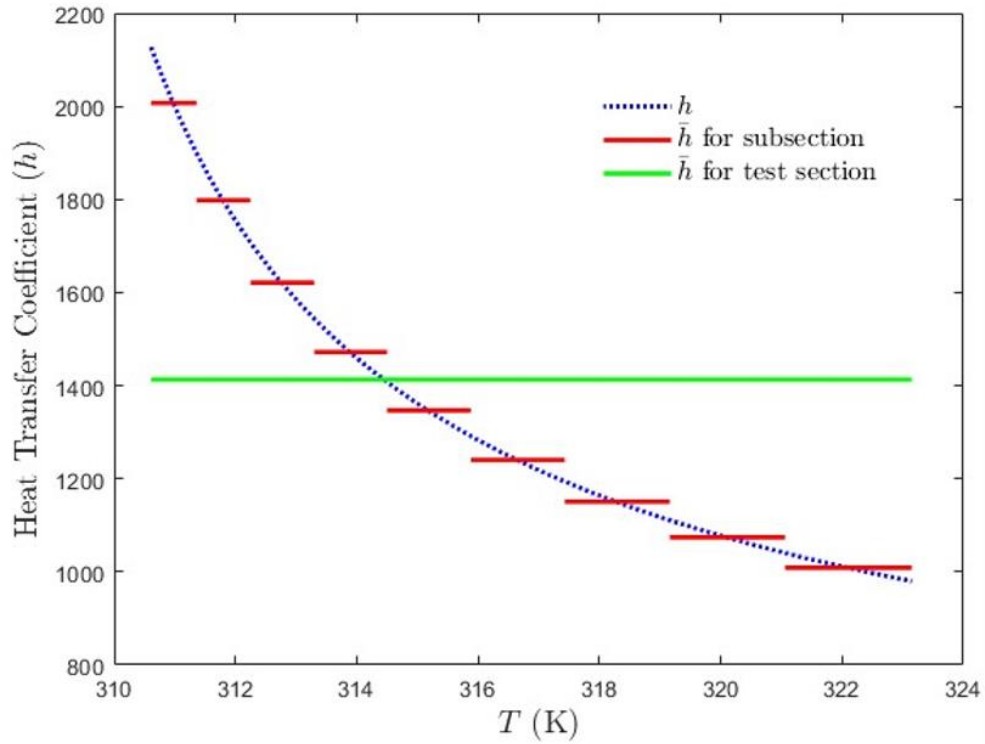


Figure 3.9 Test Section overall average heat transfer coefficient ( $\bar{h}$ ), mean heat transfer coefficient for each subsection ( $\bar{h}$ ), and heat transfer coefficient for the range of operating temperatures ( $h$ ).

### 3.6 Test Matrix

The different test runs for the experiment are specified on Table 3.2. The mass flux ( $G$ ) and heat flux ( $q''$ ) values are set to match the ones from Dang and Hihara [21] and serve for purpose of validation. Additionally, extra tests are conducted at different pressures in order to obtain supplementary data. For the different experimental conditions, the inlet temperature of the test section was varied from 30°C to 70°C, again following the procedure for Dang and Hihara experiment [21].

Table 3.2 Test matrix.

Inner diameter $d$ ( $mm$ )	Mass flux $G$ ( $kg/m^2s$ )	Heat flux $q_w''$ ( $kW/m^2$ )	Pressure $P$ ( $MPa$ )		
			8	9	10
6	200	6	Run 1	Run 2	Run 3
		12	Run 4	Run 5	Run 6
		24	Run 7	Run 8	Run 9
		33	Run 10	Run 11	Run 12
	400	12	Run 13	Run 14	Run 15

### 3.7 Assumptions Made and Limitations

While collecting data, several assumptions were made, and certain limitations were encountered. The following section will focus on summarizing them.

#### 3.7.1 Total Heat Transferred Calculations

In order to obtain the total amount of heat transferred from one fluid to another recorded experimentally, energy balance on the CO<sub>2</sub> side was used. This opposes the procedure used by Dang and Hihara, which uses energy balance on the water side. The low heat fluxes at which testing was conducted produced low temperature changes in the water, making the uncertainty of the RTDs give inaccurate results for  $\Delta T_{H_2O}$ .

Additionally, when the heat capacity for each of the fluids is calculated at inlet and outlet conditions, it is determined that the minimum heat capacity appears at the CO<sub>2</sub> inlet. Hence, the CO<sub>2</sub> inlet temperature limits the maximum amount of heat that can be transferred between fluids, since it defines the pinch point for the counterflow heat exchanger configuration.

### 3.7.2 Test Section Pressure Drop Calculations

For the purpose of our experiment, the pressure across the test section was considered constant. The pressure transducers at the inlet and outlet of the test section have an uncertainty of  $\pm 0.25\%$ . At a testing pressure of 1,160 psi (8 MPa), the uncertainty corresponds to  $\pm 2.9$  psi. The estimated pressure drop across the test section is 1 psi or less for all the test cases. Since the expected  $\Delta P$  is within the instrumentation uncertainty, the experimental results can't confidently predict its value. It is recommended that a high accuracy differential pressure transducer is implemented in the next iteration of the test section design in order to eliminate this issue.

### 3.7.3 Cooling and Pump Performance Limitations

The current loop design does not incorporate a cooling system after the test section and before the pump, since the coil and constant temperature bath assembly was used as the pre-heater. This decision was made after the initial design for the preheater consisting of a Nichrome heating wire wrapped around a copper tube failed. Thus, the  $q$  added to the system in the pre-heater has to be the same as the  $q$  removed in the test section in order to maintain thermal equilibrium in the system. From the maximum heat flux study shown in the results chapter, the current test section configuration is expected to be able to achieve heat fluxes of up to  $83 \text{ kW/m}^2$  with the  $\text{CO}_2$  under cooling conditions, removing 782.25 W from the system. This value limits the amount of heat that can be added back into the  $\text{CO}_2$  with the pre-heater. Despite of this constraint, it is still possible to replicate all the testing heat fluxes from Dang and Hihara [21], varying between 6 and  $33 \text{ kW/m}^2$ .

Nevertheless, the lack of a cooling subsystem before the pump limits its performance. Reducing the  $\text{sCO}_2$  temperature from testing conditions to lower values, allows to achieve a more viscous fluid which increases pump performance and the mass flux values that can be produced. For the selected test matrix, mass fluxes of 200 and  $400 \text{ kg/m}^2\text{s}$  were aimed to be tested. The lower value of  $200 \text{ kg/m}^2\text{s}$  can be reached with the current loop set up for  $\text{CO}_2$  inlet temperatures varying

from 30°C to 50°C; higher inlet temperature would require lowering the sCO<sub>2</sub> temperature further after the test section. Additionally, in order to collect data at a mass flux of 400 kg/m<sup>2</sup>s a cooling subsystem is required.

#### **3.7.4 Thermal Buckling and Cyclic Loading**

In order to collect all the data for this thesis work a total of 15 tests at supercritical conditions and 6 tests at subcritical conditions were required. The length of these tests varied depending on the goal for each of them, but the average length for a single test was around 120 min. This creates different stresses on the components caused by cyclical pressurization and depressurization, as well as from exposure to high pressures and thermal loads for prolonged periods of time. A lot of experimental papers in the heat exchanger literature fail to talk about thermal and cyclic loading and focus just on their experimental results. However, the effects of these loads and the number of testing iterations caused some of the instrumentation and components to wear down, without compromising the integrity of the flow loop. For instance, some of the thermocouples used to measure the outer wall temperature of the copper tube detached from the surface due to the cooling water pulling from them. The thermocouples remained attached and properly working throughout the first tests conducted. However, after being exposed to high water mass flows for extended periods of time, 7 out of the 20 thermocouples detached or stopped working. None of these 7 thermocouples were at the same location; thus, the decision of increasing measurement redundancy on the experiment and having 2 thermocouples at each longitudinal location paid off.

Additionally, thermal buckling was observed on the test section copper tube. The high pressures combined with the different heat fluxes underwent by the tube caused it to slightly bend. Figure 3.10 and Figure 3.11, show this bending, where the copper tube seems to be centered with respect to the acrylic tube on the side of the test section (Figure 3.10); whereas, in the middle part (Figure 3.11) the copper tube seems to have bent upwards and the space between copper and

acrylic is reduced on the top part and increased on the bottom. The cause of this phenomenon hasn't been clearly identified and further analysis is recommended to find out why it happened and how it can be prevented.

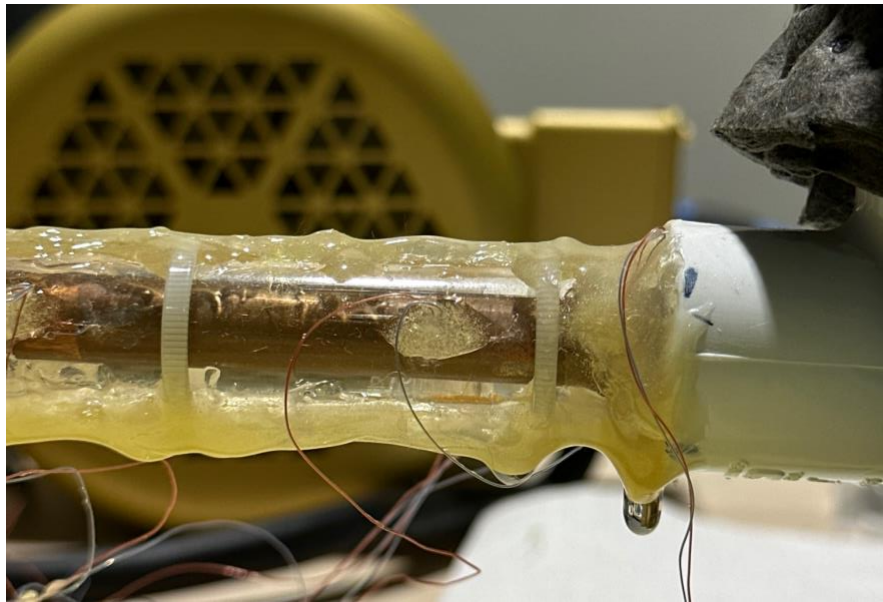


*Figure 3.10 Right side of test section copper tube.*

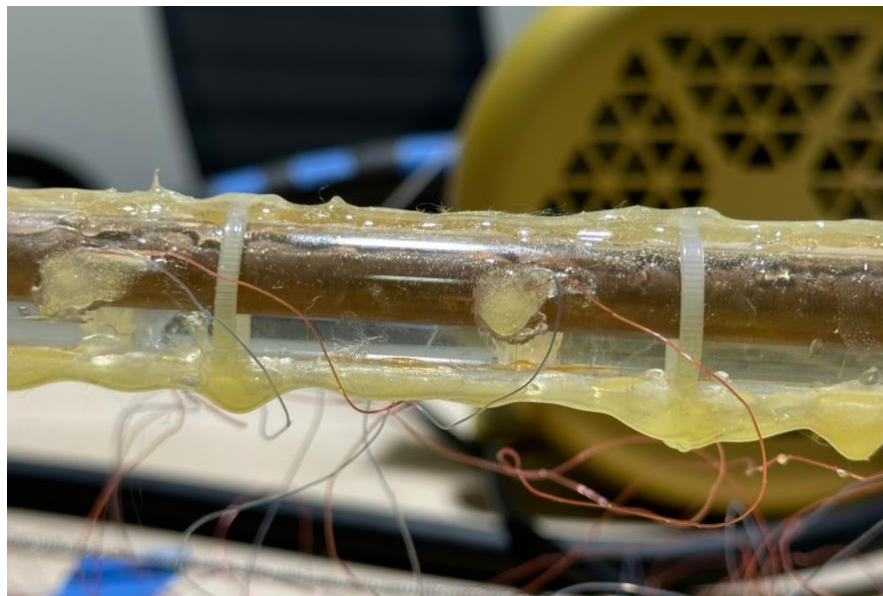


*Figure 3.11 Middle of test section copper tube.*

## **4 Results and Discussion**

The results section of this thesis is structured into two pivotal subsections, namely analytical results and experimental findings. The analytical segment examines numerical models and pretest predictions tools, providing insight into the behavior of sCO<sub>2</sub> under various conditions, as well as the projected performance of the experimental capabilities. Conversely, the experimental component explains the practical outcomes obtained through rigorous laboratory testing and measurements, offering empirical validation and enhancing the understanding of theoretical predictions. Through this dual approach, a comprehensive understanding of sCO<sub>2</sub> heat transfer behavior as well as the test rig performance and limitations is developed, laying the foundation for future experimental research for sCO<sub>2</sub> at ERAU's Thermal Science Lab.

### **4.1 Analytical Results**

The analytical results subsection is segmented into three distinct components: pretest predictions, examination of water mass flow effects on boundary conditions, and determination of the maximum attainable heat flux within the constraints of the testing facilities.

#### **4.1.1 Pretest Prediction Code Output**

As previously mentioned, the pretest prediction code is used to set up the operating conditions for the flow loop and to calculate the flow properties at different critical locations, as well as to assure safe operation of all components. Table 4.1 shows an example output from the code for the flow loop operating conditions for Run 10; with a pressure of 8 MPA and a test section inlet temperature of 50°C (323.15 K). The required operational parameters to achieve a steady state, constant heat flux, cooling boundary condition at the test section under these conditions are calculated by the tool. These settings, result in a pre-heater power of 221.5 W, a bath water temperature of 20°C (293.15 K), and a water inlet temperature of 13.6°C (286.75 K) for the test

section with a mass flow of 0.07 kg/s. In addition, the pump will need to make up for a total pressure loss of 308.10 Pa across the flow loop.

*Table 4.1 Flow loop operating conditions for test section inlet conditions of  $P = 8 \text{ MPa}$ ,  $T = 50^\circ\text{C}$ ,  $d = 6 \text{ mm}$ ,  $G = 200 \text{ kg/m}^2\text{s}$ , and  $q_w'' = 33 \text{ kW/m}^2$ .*

<b>Sections</b>	<b>Temp. Inlet (K)</b>	<b>Temp. Outlet (K)</b>	<b>Pressure Inlet (MPa)</b>	<b>Pressure Outlet (MPa)</b>
<b>Test Section</b>	323.15	310.61	8.0000	7.9998
<b>Piping</b>	310.61	310.61	7.9998	7.9998
<b>Const. Temp. Bath</b>	310.61	293.25	7.9998	7.9998
<b>Piping</b>	293.25	293.25	7.9998	7.9998
<b>Pump</b>	293.25	293.25	7.9998	8.0001
<b>Piping</b>	293.25	293.25	8.0001	8.0001
<b>Pre-Heater</b>	293.25	323.2	8.0001	8.0001
<b>Piping</b>	323.2	323.2	8.0001	8.0000
<b>Flow Meter</b>	323.2	323.2	8.0000	8.0000
<b>Piping</b>	323.2	323.2	8.0000	8.0000

The tool also generates a profile of the temperature variations for CO<sub>2</sub> and water along the test section. This allows to examine the counterflow heat exchanger behavior of the test section as well as its constant heat flux boundary condition. Figure 4.1 simulates the change in CO<sub>2</sub> and water temperature throughout the test section for the previously described case. It is important to notice that the sCO<sub>2</sub> temperature does not vary linearly, due to the strong gradients in thermophysical properties around the critical point.

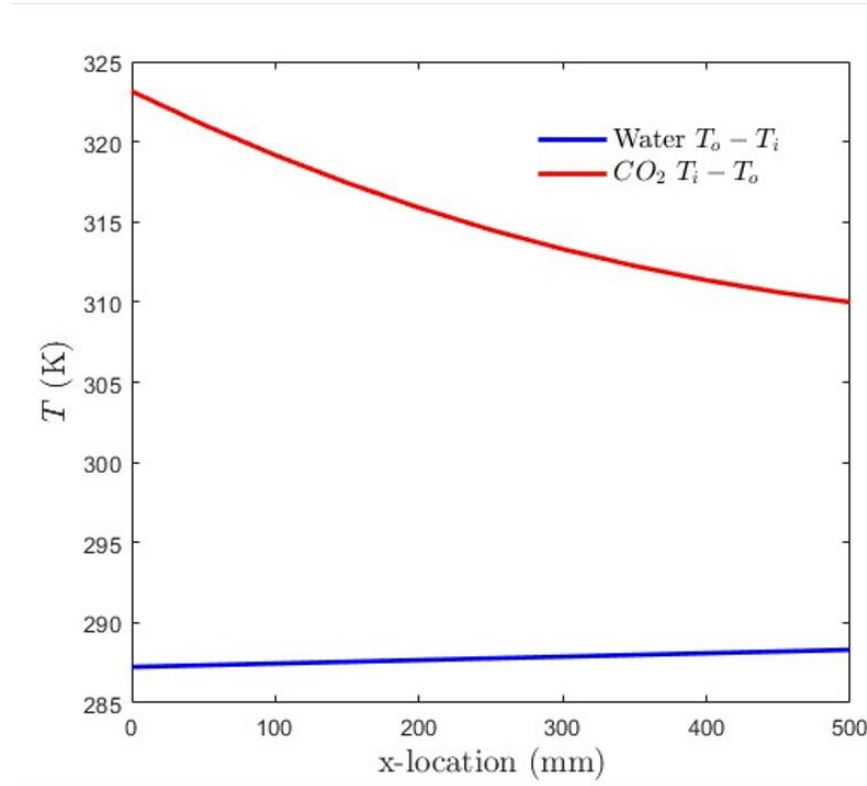


Figure 4.1 Change in  $CO_2$  and water temperature with respect to  $x$ -location for test section inlet conditions of  $P = 8$  MPa,  $T = 50^\circ\text{C}$ ,  $d = 6$  mm,  $G = 200$  kg/m<sup>2</sup>s, and  $q_w'' = 33$  kW/m<sup>2</sup>.

#### 4.1.2 Water Mass Flow Effect

The computational tool was used for a preliminary study on how the water mass flow affects the test section boundary condition. It was found that a lower mass flow for the water jacket resembles the operation of a constant heat flux heat exchanger, whereas a high water mass flow acts as a constant temperature boundary condition. Figure 4.2 shows the counterflow heat exchanger diagram for several mass flow cases. In the case of Dang and Hihara [21] experiment, a constant heat flux was assumed for the test section; thus, lower water mass flows were used during experimental testing. Additionally, having lower water mass flows, increases  $\Delta T_{H_2O}$  reducing the level of uncertainty caused by the water RTDs.

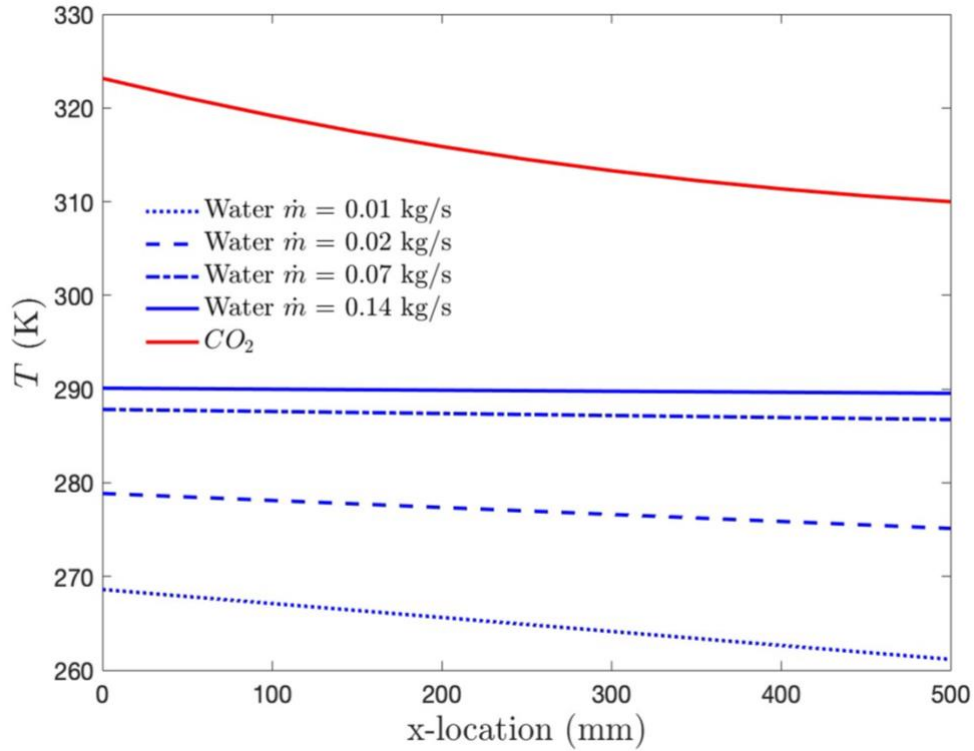
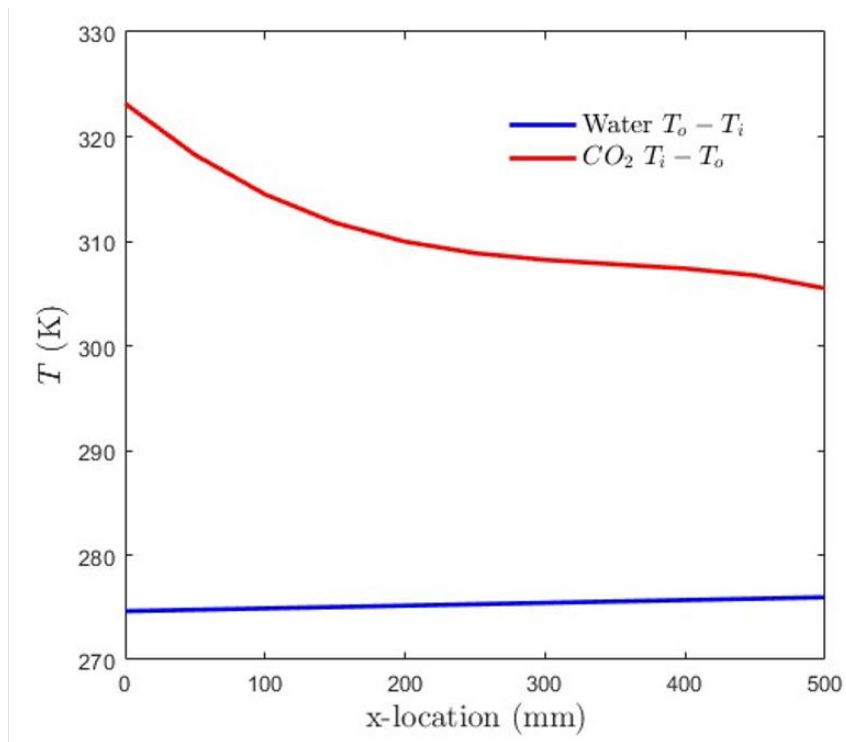


Figure 4.2 Test section counterflow heat exchanger simulation for different water mass flows ( $\dot{m}$ ) for test section inlet temperatures of  $P = 8$  MPa,  $T = 50^\circ\text{C}$ ,  $d = 6$  mm,  $G = 200$  kg/m<sup>2</sup>s, and  $q_w'' = 33$  kW/m<sup>2</sup>.

#### 4.1.3 Maximum Heat Flux Study

The analysis code was also used for a study on the maximum heat fluxes that can be achieved with the current experimental set up under heating and cooling conditions. Different testing scenarios were run varying water and CO<sub>2</sub> inlet temperatures and water mass flow, while keeping operating pressure and CO<sub>2</sub> mass flow constant for easier comparison; allowing to find the optimal control settings to reach the highest possible heat fluxes. With the CO<sub>2</sub> under cooling conditions, the estimated maximum heat flux achievable with the current loop set up is 83.0 kW/m<sup>2</sup> and it corresponds to a CO<sub>2</sub> inlet temperature of 50°C (323.15 K) and a water inlet temperature of 1.48°C (274.14 K), while the CO<sub>2</sub> and H<sub>2</sub>O mass flows were taken as 0.0057 kg/s ( $G = 201.60$  kg/m<sup>2</sup>s) and 0.14 kg/s, respectively, while operating the loop at 8 MPa. Figure 4.3, simulates the

temperature profile for CO<sub>2</sub> and H<sub>2</sub>O along the test section for the maximum heat flux cooling case. In this scenario, the maximum heat flux that can be achieved under cooling conditions is limited by the water inlet temperature and the water mass flow. The highest possible water mass flow was considered to be 0.14 kg/s, since greater values could damage or detach the thermocouples inside of the test section. On the other hand, by using water as the cooling fluid, we are limited by the freezing point of water at 0°C. If other cooling fluids were to be used in the water circulator, for instance, a water/glycol mixture, higher heat flux values could be achieved.



*Figure 4.3 Test section counterflow heat exchanger simulation for maximum heat flux cooling case.*

When heating the CO<sub>2</sub>, we are limited by the maximum temperature of the water heating the CO<sub>2</sub>. The water circulator has a maximum operating temperature of 80°C with water as the heat transfer fluid. However, using mineral/silicone oils increases the operating temperature to 200°C,

which would allow for higher heat fluxes. The maximum estimated heat flux possible with the current loop configuration is 108.0 kW/m<sup>2</sup>. In order to achieve this state, the CO<sub>2</sub> inlet temperature needs to be set to 22°C (295.15 K) and the water inlet temperature to 80.34°C (353.49 K) while the mass flows required are 0.0057 kg/s ( $G = 201.60 \text{ kg/m}^2\text{s}$ ) for the CO<sub>2</sub> and 0.14 kg/s for the H<sub>2</sub>O. The pressure was kept at 8 MPa. Figure 4.4, reproduces the change in temperature of both fluids along the test section counterflow heat exchanger.

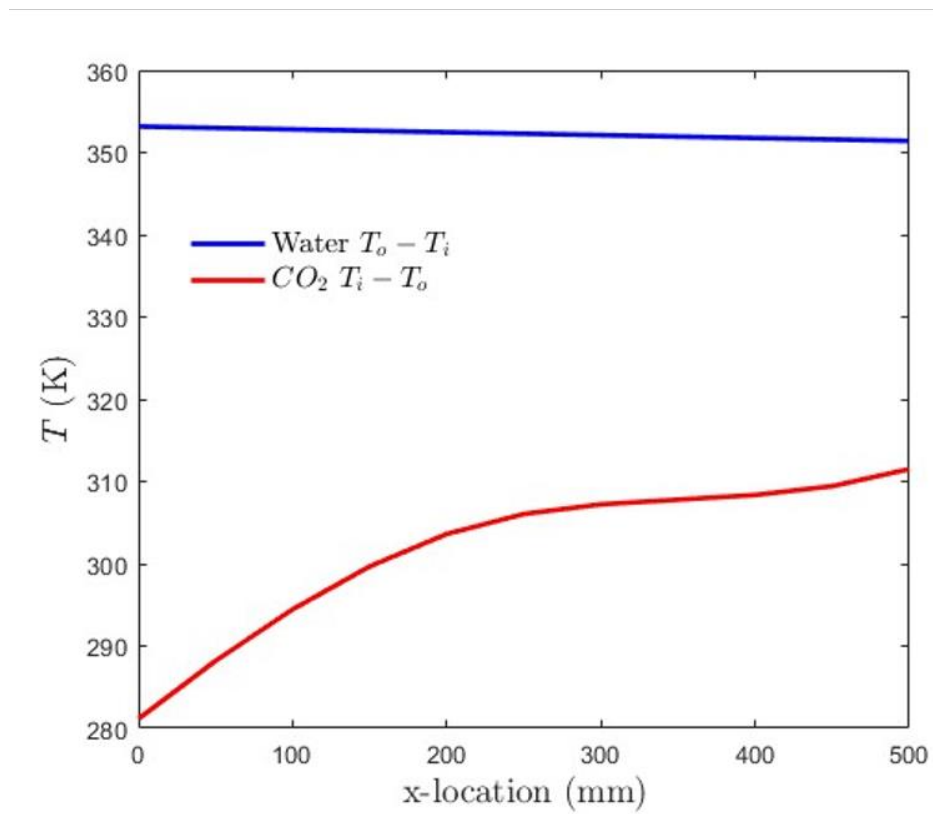


*Figure 4.4 Test section counterflow heat exchanger simulation for maximum heat flux heating case.*

## 4.2 Experimental Results

The experimental results subsection explores the performance of different components in the experimental flow loop, enhancing the understanding of the testing capabilities as well as its limitations and areas of improvement. Additionally, it documents the benchmarking efforts and records the outcomes of the flow loop validation process for subcritical and supercritical conditions.

### 4.2.1 Water Loop Heat Leakage

Due to the nature of the experiment, correctness on the temperature readings for the water loop is crucial to obtain proper results. Since the  $\Delta T_{H_2O}$  is used to calculate the total amount of heat transferred between both fluids, the amount of heat loss to the environment needs to be accounted for. In order to do so, the water loop was run independently, with no CO<sub>2</sub> flowing in the inner tube, and the change in water temperature as well as the heat loss were calculated. When running the water at typical testing mass flows of around 0.05 kg/s, the  $\Delta T_{H_2O}$  was found to be +0.0355°C resulting in a heat loss of  $q_{loss} = 7.427$  W, considered almost negligible for the experiment. Figure 4.5 shows the  $\Delta T_{H_2O}$  at steady-state conditions, when the water loop was operating at 15°C and mass flow of 0.05 kg/s. However, it was found out that when the water mass flow was further reduced by choking the flow, the water becomes stagnant through the hose, indicating that the water circulator can't make up for the pressure drop, and resulting in higher losses to the environment. Thus, in order to obtain accurate results, it is recommended to keep the water mass flow above 0.05 kg/s.

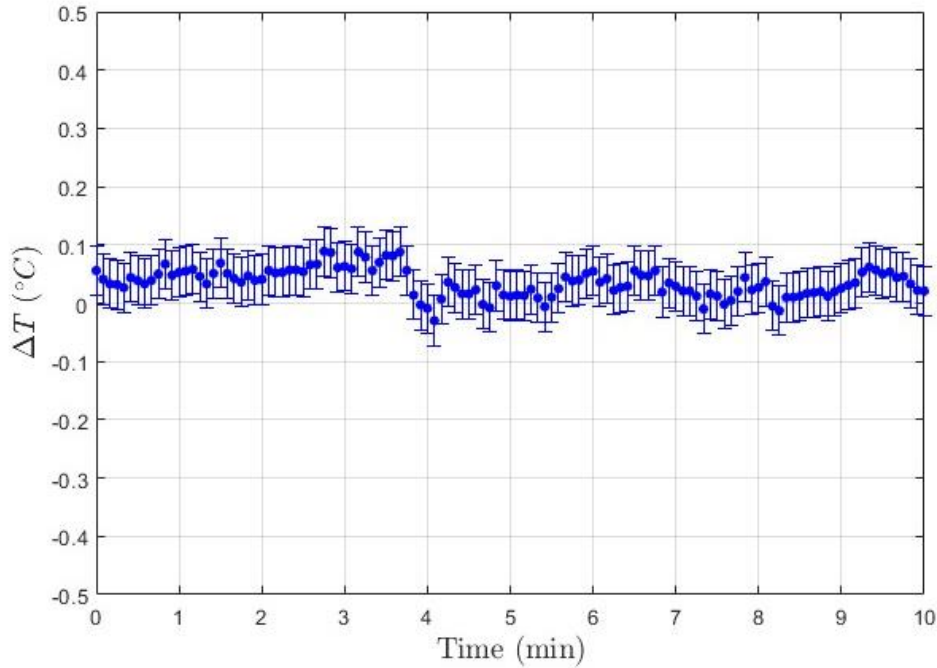


*Figure 4.5  $\Delta T_{H_2O}$  and uncertainty levels for steady-state conditions at a water inlet temperature of 15°C.*

#### **4.2.2 Accumulator Performance**

When operating the flow loop, the changes in sCO<sub>2</sub> temperature inside the loop may cause a change in internal pressure. In order to tackle this problem, a pressure accumulator charged with Nitrogen was used. It was found out, that the accumulator needs to be charged to a pressure between 1/2 and 3/4 of the testing pressure. For example, if the desired operating pressure is 1,305 psi (9 MPa) the accumulator needs to have an internal pressure between 652.5 and 978.75 psi. Thus, the accumulator needs to be charged before every test based on the test case that is run. Figure 4.6 shows the increase in pressure inside of the test rig when the accumulator is below the indicated range. In this case, the pressure climbed up from 1,160 psi (8 MPa) to 1,450 psi (10 MPa) when the sCO<sub>2</sub> temperature went from room temperature (21.5°C) to the desired testing temperature of 35°C.

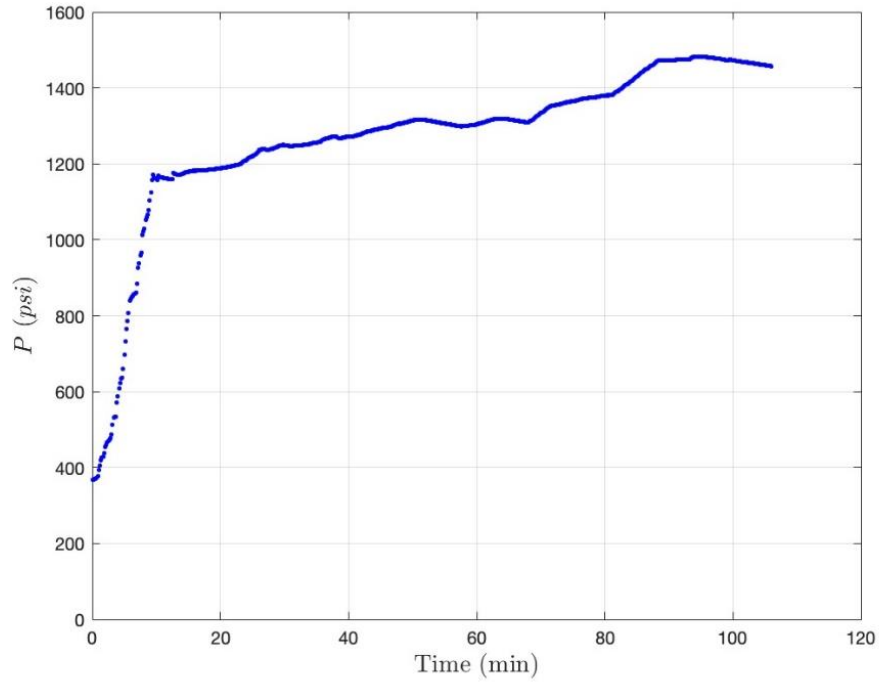


Figure 4.6 Flow loop internal pressure variations when accumulator is charged below the recommended pressures.

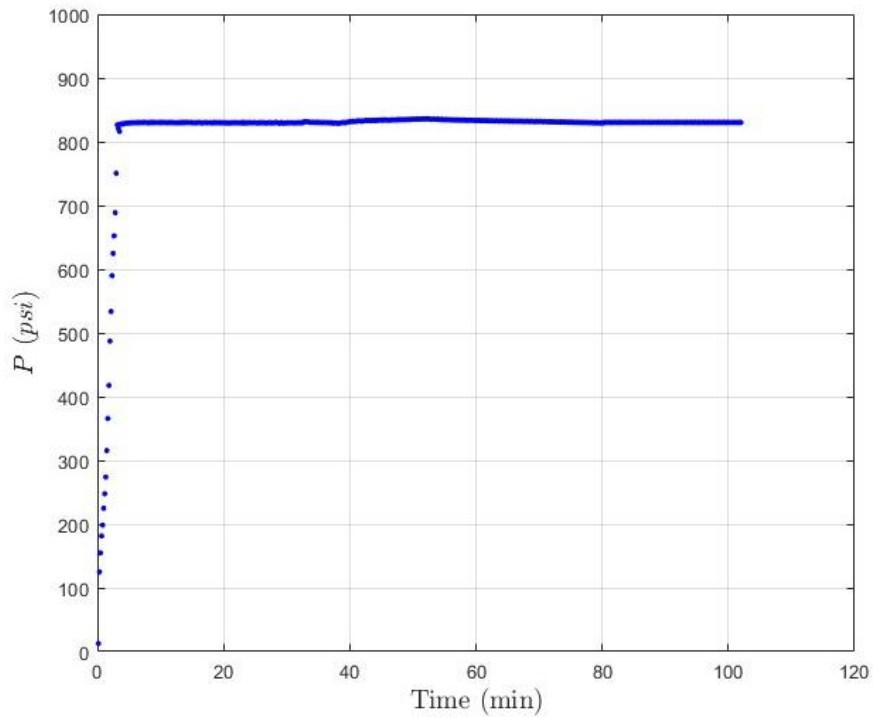


Figure 4.7 Flow loop internal pressure variations when accumulator is charged inside the recommended values.

On the other hand, Figure 4.7 displays the system pressure during a different test where the CO<sub>2</sub> temperature was raised from room temperature to 33.5°C. For this test, the accumulator was charged to a pressure of 600 psi, which allowed to keep the testing pressure constant at 830 psi.

#### **4.2.3 Pump and Flow Meter Performance**

The magnetically driven gear pump utilized on the experiment is not intended for fluids with viscosities below 1 cp (0.001 Pa·s); however, the experimental conditions covered by this paper do not surpass 0.072 cp ( $7.2 \times 10^{-5}$  Pa·s) when operating the pump with sCO<sub>2</sub>. Thus, since pump curves for the current pump at such low viscosities do not exist, a pump characterization study is required. Due to time constraints and problems with the Coriolis mass flow meter during the first months of the study, this task does not fall under the scope of this work. During testing, the pump power was adjusted ad libitum, in order to obtain the desired mass flows. However, different tests dedicated to study the performance and capabilities of the pump under subcritical and supercritical conditions were carried. Figure 4.8 shows the mass flow values achieved under different pump RPM settings while maintaining isothermal conditions in the loop at 22.5°C and 780 psi. Under these conditions, CO<sub>2</sub> exists in gas state, presenting very low viscosity values. However, the changes in RPM clearly induce changes in mass flow, that are successfully recorded by the Coriolis mass flow meter, underlining the proper operation of the component. Additionally, the pump is able to hold these mass flows constant over time, allowing for steady-state conditions inside of the flow loop.

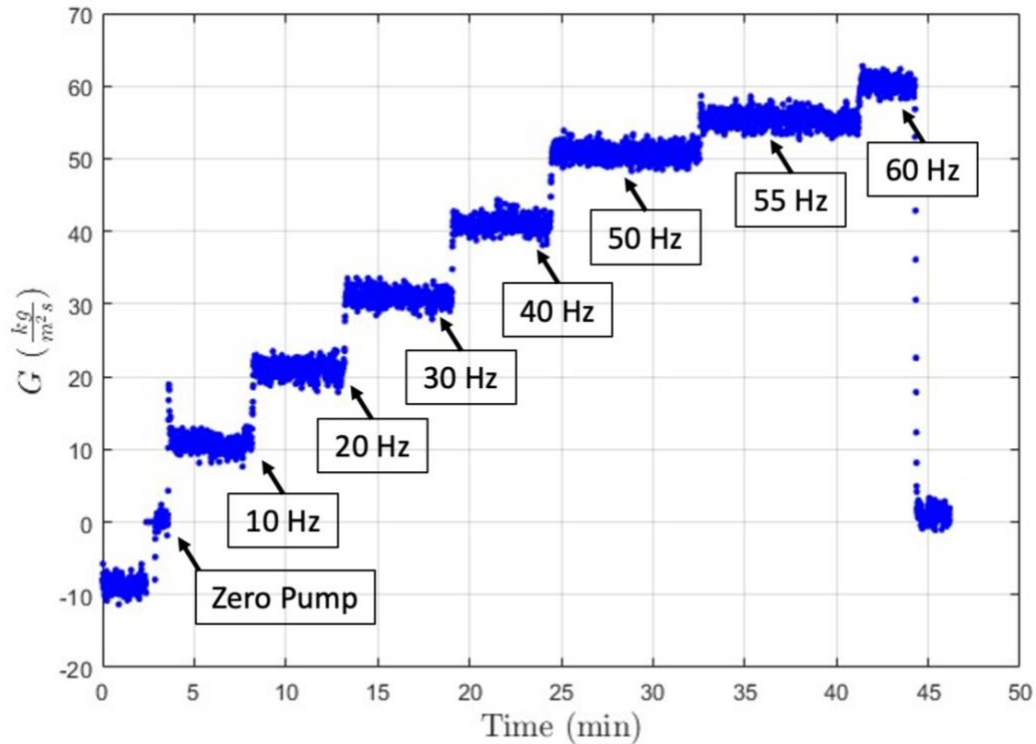
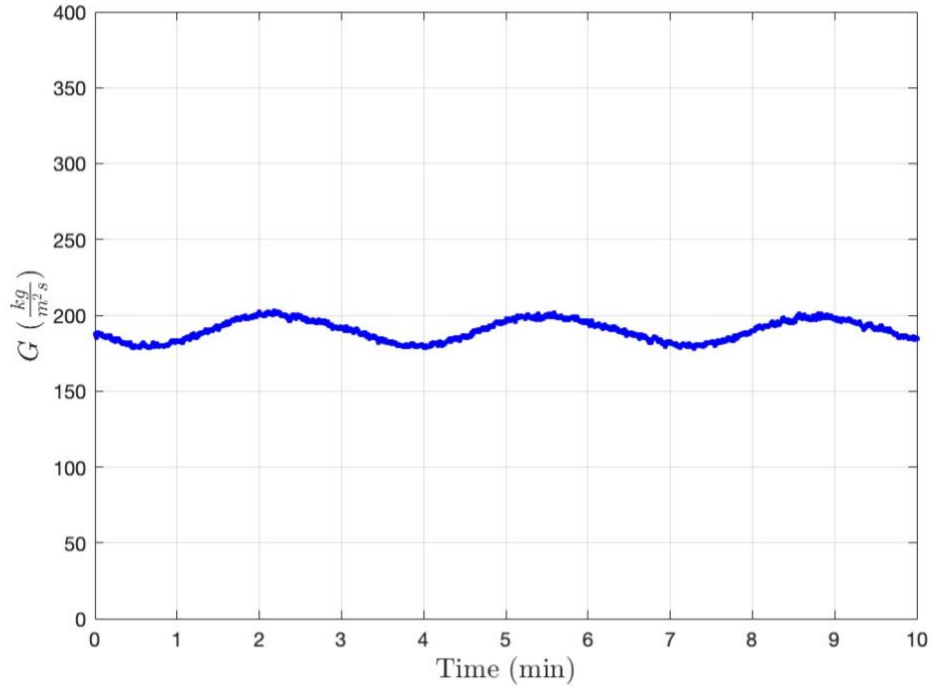


Figure 4.8 Gear pump performance under isothermal conditions and different RPM settings for  $P = 780$  psi and  $T = 22.5^\circ\text{C}$ .

During supercritical testing, the target mass flux was  $G = 200$   $\text{kg}/\text{m}^2\cdot\text{s}$ . The higher density of  $\text{CO}_2$  in supercritical conditions considerably improved the pump efficiency, allowing to reach the intended mass flux while running at 57 Hz (3,420 RPM). Figure 4.9 shows how the required mass flux was reached and maintained constant for one of the supercritical runs. Additionally, the higher densities got rid of some of the noise that was recorded by the Coriolis mass flow meter when the  $\text{CO}_2$  was flowing in gaseous state.

The maximum  $G$  that can be achieved with the experimental set up is still unknown. During the tests conducted, the  $\text{sCO}_2$  was kept at higher temperatures (more gas-like properties) since the constant temperature bath (sub-cooler) hadn't yet been added to the loop. Once this component is

introduced, it will be possible to lower the sCO<sub>2</sub> temperature aft the test section and before the pump, resulting in a more viscous, liquid-like fluid that will allow to reach higher mass flux values.



*Figure 4.9 CO<sub>2</sub> targeted mass flux ( $G = 200 \text{ kg/m}^2\text{s}$ ) recorded by the Coriolis mass flow meter at steady-state conditions.*

#### 4.2.4 Subcritical Validation

The experimental results are compared to trusted traditional correlations in order to validate the rig design for subcritical conditions. The average heat transfer coefficient ( $\bar{h}$ ) for the test section is compared to Gnielinki's correlation. To validate the loop for subcritical states, 3 cases with CO<sub>2</sub> in gas state were conducted. One test was performed with the CO<sub>2</sub> under heating conditions, and the other two under cooling conditions. A summary of the three cases can be seen in Table 4.2.

Table 4.2 Subcritical tests results.

Measurement	Test Heating	Test Cooling 1	Test Cooling 2
$T_{CO_2}$ inlet (°C)	24.95	29.27	30.17
$T_{CO_2}$ outlet (°C)	33.22	15.91	16.10
$T_{H_2O}$ inlet (°C)	39.25	9.91	10.00
$T_{H_2O}$ outlet (°C)	38.83	10.08	10.20
$\dot{m}_{H_2O}$ (kg/s)	0.0499	0.499	0.421
$\dot{m}_{CO_2}$ (kg/s)	0.0015	0.0009	0.0011
$G$ (kg/m <sup>2</sup> s)	52.33	33.02	37.83
$P$ (MPa)	5.72	4.28	4.29
$q''$ (kW/m <sup>2</sup> )	2.96	2.09	2.51
$\bar{h}$ (W/m <sup>2</sup> K)	318.7	179.03	208.84
% difference with <i>Gnielinski correlation</i>	1.36%	7.78%	12.14%

As shown in Figure 4.10, all three cases present a percent difference with Gnielinski's correlation lower than 20%, validating our loop for subcritical conditions and laying the groundwork for supercritical validation.

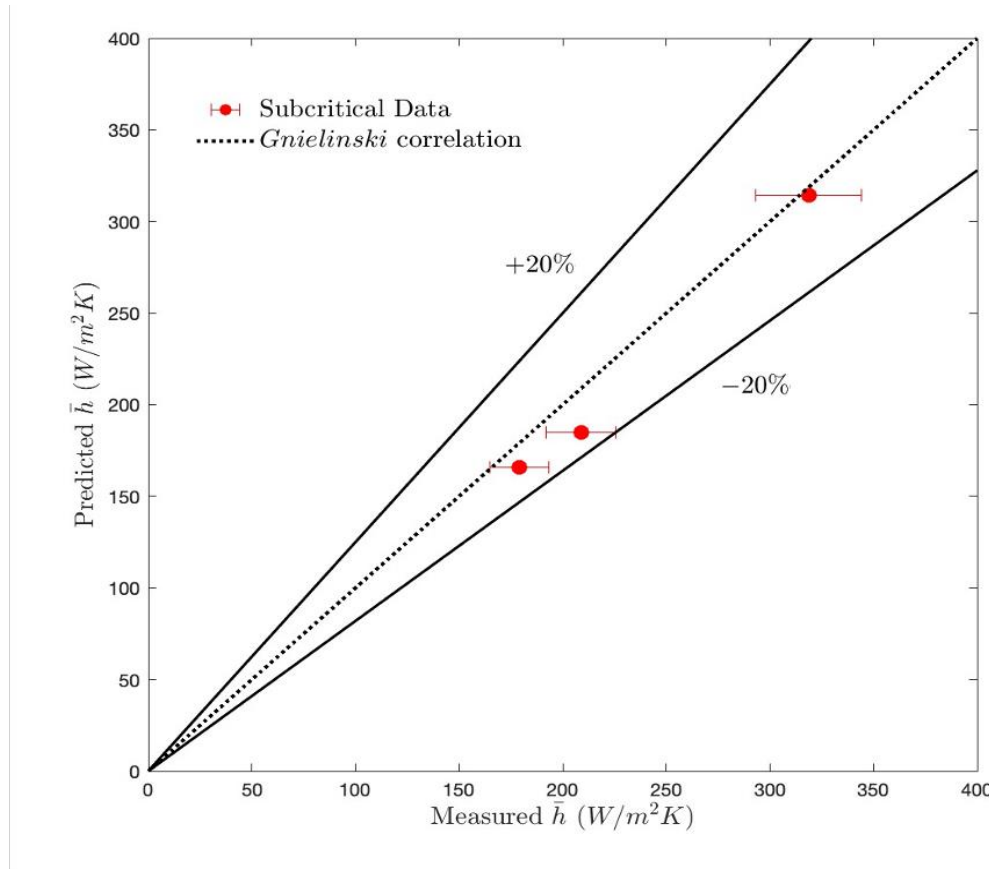


Figure 4.10 Subcritical results for average heat transfer coefficient ( $\bar{h}$ ) compared to Gnielinski correlation.

#### 4.2.5 Supercritical Validation

Once the loop was characterized and validated for subcritical conditions, supercritical validation against Dang and Hihara’s study could be completed. Table 4.3 summarizes the three testing scenarios used for validation. All of them were completed at pressures of 9 MPa and mass fluxes of 200 kg/m<sup>2</sup>s. Due to the lack of a sub-cooler after the test section, the sCO<sub>2</sub> inlet temperatures were kept below 40°C, in order to be able to reach the desired mass flux values with the current pump system. Test 1 and Test 2 correspond to Run 5 on the test matrix, while Test 3 corresponds to Run 8.

Table 4.3 Supercritical test results.

Measurement	Test 1	Test 2	Test 3
$T_{CO_2}$ inlet (°C)	30.83	35.01	40.26
$T_{CO_2}$ outlet (°C)	25.03	30.78	36.32
$T_{H_2O}$ inlet (°C)	16.47	20.40	30.04
$T_{H_2O}$ outlet (°C)	17.01	21.61	30.83
$\dot{m}_{H_2O}$ (kg/s)	0.0502	0.0499	0.0499
$\dot{m}_{CO_2}$ (kg/s)	0.0059	0.0061	0.0054
$G$ (kg/m <sup>2</sup> s)	208.62	215.99	189.99
$P$ (MPa)	9.04	8.87	9.05
$q''$ (kW/m <sup>2</sup> )	12.58	13.52	21.57
$\bar{h}$ (W/m <sup>2</sup> K)	1,156.27	1,177.97	2,882.03
% <i>difference with D&amp;H correlation</i>	19.32 %	26.08 %	19.56 %

The agreement between the experimental data and Dang and Hihara [21] modified Gnielinski correlation can be seen in Figure 4.11. When considering the uncertainty, all data points fall inside  $\pm 20\%$  of the predicted values, which is the level of accuracy that Dang and Hihara [21] found for their correlation when compared to their experimental data. Thus, benchmarking against Dang and Hihara's experiment at supercritical conditions was deemed successful for the test cases run.

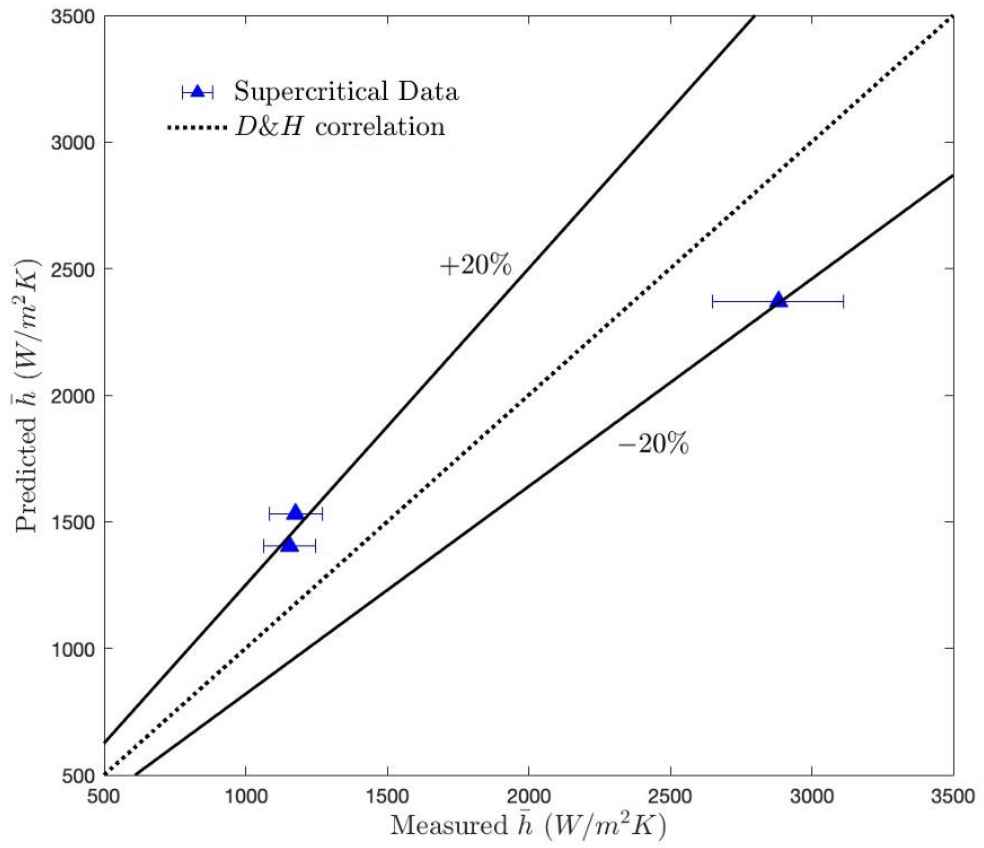


Figure 4.11 Supercritical results for average heat transfer coefficient ( $\bar{h}$ ) compared to Dang and Hihara correlation.

## 5 Conclusions and Recommendations

The designed rig establishes heat transfer research capabilities for sCO<sub>2</sub> at ERAU's Thermal Science Lab, serving as the foundation to conduct future sCO<sub>2</sub> experiments with testing conditions up to 1,500 psi (10.34 MPa) and 85°C (353.15 K). The flow loop is currently built, and pressure tested for supercritical conditions, and it has been validated for subcritical and supercritical cases. The experimental data is compared against the results from Dang and Hihara [21] and all conducted tests fall within ±20% of the predicted values, allowing for the commissioning of the flow loop. The analytical tool for pretest predictions is used to adjust the operational conditions of the different components and guarantee the integrity of rig during testing. The tool will be further refined in order include Dang and Hihara's correlation [21] and to become user friendly so other researchers are able to use it for future experiments. Lastly, numerical CFD simulations will be conducted with the actual rig geometry in the following months to further substantiate the validity of the designed flow loop.

### 5.1 Recommendations and Future Work

Due to time constraints and unforeseen complications with some of the equipment, only a limited amount of supercritical data was collected. It is recommended that the loop is tested for more cases, as described by the test matrix in Table 3.2. This will increase the confidence in the experimental results for a wider range of operating conditions. However, the cases that were tested, matched the data in the literature with a percent difference within 20%.

The first upgrade that should be implemented into the test rig is adding a cooling system between the outlet of the test section and the inlet of the pump. The recommended design is a coil submerged in a constant temperature bath that allows to lower the sCO<sub>2</sub> temperature before going back into the pump. This will increase pump performance and allow for a wider variety of mass fluxes to be tested. The goal should be reaching a mass flux of 400 kg/m<sup>2</sup>s for pressures between

8 to 10 MPa, and CO<sub>2</sub> inlet temperatures between 30°C to 70°C. Thus, the cooler should be able to bring the supercritical CO<sub>2</sub> temperature down from around 70°C to liquid state at 10°C. Adding a sub-cooler would also help to characterize the pump and create pump curves for supercritical CO<sub>2</sub>, something novel that hasn't been covered by the literature yet.

Another improvement that should be carried out is adding a differential pressure transducer to the test section. Due to the high uncertainties in the pressure transducers used, along with the high testing pressures, it was not possible to measure the pressure drop across the test section in an accurate way. The differential pressure sensor must be rated for pressures up to 1,500 psi and have a resolution lower than 1 psi. These requirements make the sensor hard to install and expensive; thereby, not viable for the first loop design iteration.

The way the loop is pressurized should also be an area of improvement. Charging the loop directly from the storage tank with a pressure regulator requires the tank to have a higher pressure than the desired testing pressure. Additionally, if another coil is introduced in the design as the cooling system the loop volume would considerably increase, and this, in turn, would increase the amount of CO<sub>2</sub> used. Adding a pressurization system would allow to save CO<sub>2</sub> and reduce the testing costs.

All these improvements would lead to the design of a novel test section. The new test section will be easily replaced by the current one. The thermal buckling issues will be tackled and new, more accurate ways of measuring local outer wall temperatures will be introduced. Temperature sensitive paint has been proposed as an ideal candidate capable of measuring temperature profiles and local heat transfer along the test section in a more precise way.

## 6 REFERENCES

- [1] Xu, J., Yang, C., Zhang, W., and Sun, D., “Turbulent convective heat transfer to CO<sub>2</sub> in a helical tube at near-critical pressure,” *International Journal of Heat and Mass Transfer*, Vol. 80, 2015, pp. 748–758. <https://doi.org/10.1016/j.ijheatmasstransfer.2014.09.066>.
- [2] Xiang, B., Patra, P. K., Montzka, S. A., Miller, S. M., Elkins, J. W., Moore, F. L., Atlas, E. L., Miller, B. R., Weiss, R. F., Prinn, R. G., and Wofsy, S. C., “Global emissions of refrigerants HCFC-22 and HFC-134a: Unforeseen seasonal contributions,” *Proceedings of the National Academy of Sciences*, Vol. 111, 2014, pp. 17379–17384. <https://doi.org/10.1073/pnas.1417372111>.
- [3] Hafner, A., and Banasiak, K., “R744 ejector technology future perspectives,” *Journal of Physics: Conference Series*, Vol. 745, 2016, p. 032157. <https://doi.org/10.1088/1742-6596/745/3/032157>.
- [4] Zhang, G.-W., Hu, P., Chen, L.-X., and Liu, M.-H., “Experimental and simulation investigation on heat transfer characteristics of in-tube supercritical CO<sub>2</sub> cooling flow,” *Applied Thermal Engineering*, Vol. 143, 2018, pp. 1101–1113. <https://doi.org/10.1016/j.applthermaleng.2018.07.108>.
- [5] Ahn, Y., Bae, S. J., Kim, M., Cho, S. K., Baik, S., Lee, J. I., and Cha, J. E., “Review of supercritical CO<sub>2</sub> power cycle technology and current status of research and development,” *Nuclear Engineering and Technology*, Vol. 47, No. 6, 2015, pp. 647–661. <https://doi.org/10.1016/j.net.2015.06.009>.
- [6] Dostal, Vaclav, Michael J. Driscoll, and Pavel Hejzlar. "A supercritical carbon dioxide cycle for next generation nuclear reactors." PhD diss., Massachusetts Institute of Technology, Department of Nuclear Engineering, 2004.
- [7] Turchi, C. S., Ma, Z., Neises, T. W., and Wagner, M. J., “Thermodynamic study of advanced supercritical carbon dioxide power cycles for concentrating solar power systems,” *Journal of Solar Energy Engineering*, Vol. 135, 2013. <https://doi.org/10.1115/1.4024030>.
- [8] Lorentzen, G., “The use of natural refrigerants: a complete solution to the CFC/HCFC predicament,” *International Journal of Refrigeration*, Vol. 18, No. 3, 1995, pp. 190–197. [https://doi.org/10.1016/0140-7007\(94\)00001-e](https://doi.org/10.1016/0140-7007(94)00001-e).
- [9] Sullivan, N., “On the local heat transfer behavior of supercritical carbon dioxide,” PhD thesis, Embry-Riddle Aeronautical University, Jul. 2021.
- [10] Sullivan, N. P., Chao, Y., Boetcher, S. K. S., and Ricklick, M. A., “Impact of Uncertainty on Prediction of Supercritical CO<sub>2</sub> Properties and Nusselt Numbers,” *Journal of Heat Transfer*, Vol. 143, No. 10, 2021, p. 104501. <https://doi.org/10.1115/1.4051856>.

- [11] Pitla, S., Groll, E., and Ramadhyani, S., “Convective Heat Transfer from In-Tube Cooling of Turbulent Supercritical Carbon Dioxide: Part 2- Experimental Data and Numerical Predictions,” *HVAC&R Research*, Vol. 7, 2001, pp. 367–382. <https://doi.org/10.1080/10789669.2001.10391281>.
- [12] Lopes, N., Chao, Y., Dasarla, V., Sullivan, N., Ricklick, M., and Boetcher, S., “Comprehensive Review of Supercritical CO<sub>2</sub> Correlations for Straight Tubes: A Historical Perspective,” *Journal of Heat Transfer*, Vol. 144, No. 12, 2022, p. 120801. <https://doi.org/10.1115/1.4055345>.
- [13] Crespi, F., Gavagnin, G., Sánchez, D., and Martínez, G. S., “Supercritical carbon dioxide cycles for power generation: A review,” *Applied Energy*, Vol. 195, 2017, pp. 152–183. <https://doi.org/10.1016/j.apenergy.2017.02.048>.
- [14] White, M. T., Bianchi, G., Chai, L., Tassou, S. A., and Sayma, A. I., “Review of supercritical CO<sub>2</sub> technologies and systems for power generation,” *Applied Thermal Engineering*, Vol. 185, 2021, p. 116447. <https://doi.org/10.1016/j.applthermaleng.2020.116447>.
- [15] Liu, L., Yang, Q., and Cui, G., “Supercritical Carbon Dioxide (s-CO<sub>2</sub>) Power Cycle for Waste Heat Recovery: A Review from Thermodynamic Perspective,” *Processes*, Vol. 8, No. 11, 2020, p. 1461. <https://doi.org/10.3390/pr8111461>.
- [16] Sánchez, D., Chacartegui, R., Jiménez-Espadafor, F., and Sánchez, T., “A New Concept for High Temperature Fuel Cell Hybrid Systems Using Supercritical Carbon Dioxide,” *Journal of Fuel Cell Science and Technology*, Vol. 6, No. 2, 2009. <https://doi.org/10.1115/1.3080550>.
- [17] Walnum, H. T., Neksa, P., Nord, L. O., and Andresen, T., “Modelling and simulation of CO<sub>2</sub> (carbon dioxide) bottoming cycles for offshore oil and gas installations at design and off-design conditions,” *Energy*, Vol. 59, 2013, pp. 513–520. <https://doi.org/10.1016/j.energy.2013.06.071>.
- [18] Shu, G., Shi, L., Tian, H., Li, X., Huang, G., and Chang, L., “An improved CO<sub>2</sub>-based transcritical Rankine cycle (CTRC) used for engine waste heat recovery,” *Applied Energy*, Vol. 176, 2016, pp. 171–182. <https://doi.org/10.1016/j.apenergy.2016.05.053>.
- [19] Wang, X., and Dai, Y., “An exergoeconomic assessment of waste heat recovery from a Gas Turbine-Modular Helium Reactor using two transcritical CO<sub>2</sub> cycles,” *Energy Conversion and Management*, Vol. 126, 2016, pp. 561–572. <https://doi.org/10.1016/j.enconman.2016.08.049>.
- [20] Li, W., Yu, Z., Wang, Y., and Li, Y., “Heat transfer of supercritical carbon dioxide in a tube-in-tube heat exchanger—a CFD study,” *The Journal of Supercritical Fluids*, Vol. 181, 2022, p. 105493. <https://doi.org/10.1016/j.supflu.2021.105493>.

- [21] Dang, C., and Hihara, E., "In-tube cooling heat transfer of supercritical carbon dioxide. Part 1. Experimental measurement," *International Journal of Refrigeration*, Vol. 27, No. 7, 2004, pp. 736–747. <https://doi.org/10.1016/j.ijrefrig.2004.04.018>.
- [22] Liu, M., Jiang, X., Fang, Y., Guo, M., and Ding, C., "Numerical Investigation on Convective Heat Transfer of Supercritical Carbon Dioxide in a Mini Tube Considering Entrance Effect," *Journal of Thermal Science*, Vol. 30, No. 6, 2021, pp. 1986–2001. <https://doi.org/10.1007/s11630-021-1510-8>.
- [23] Chao, Y., Lopes, N. C., Ricklick, M. A., and Boetcher, S. K. S., "Hydraulic development length and boundary condition effects on local sCO<sub>2</sub> heat transfer coefficients," *The 7th International Supercritical CO<sub>2</sub> Power Cycles Symposium*, San Antonio, Texas, 2022.
- [24] Chao, Y., Lopes, N. C., Boetcher, S., and Ricklick, M. A., "Numerical investigation of flow development and thermal boundary condition effects on local sCO<sub>2</sub> heat transfer trends in circular tubes," *AIAA SCITECH 2023 Forum, American Institute of Aeronautics and Astronautics*, 2023. <https://doi.org/10.2514/6.2023-0604>.
- [25] Liu, S., Huang, Y., Liu, G., Wang, J., and Leung, L. K., "Improvement of buoyancy and acceleration parameters for forced and mixed convective heat transfer to supercritical fluids flowing in vertical tubes," *International Journal of Heat and Mass Transfer*, Vol. 106, 2017, pp. 1144–1156. <https://doi.org/10.1016/j.ijheatmasstransfer.2016.10.093>.
- [26] Sharabi, M., Ambrosini, W., He, S., and Jackson, J., "Prediction of turbulent convective heat transfer to a fluid at supercritical pressure in square and triangular channels," *Annals of Nuclear Energy*, Vol. 35, No. 6, 2008, pp. 993–1005. <https://doi.org/10.1016/j.anucene.2007.11.006>
- [27] Li, W., and Yu, Z., "Heat exchangers for cooling supercritical carbon dioxide and heat transfer enhancement: A review and assessment," *Energy Reports*, Vol. 7, 2021, pp. 4085–4105. <https://doi.org/10.1016/j.egy.2021.06.089>.
- [28] Schmitt, J., et al. "Study of a supercritical CO<sub>2</sub> turbine with TIT of 1350 K for Brayton cycle with 100 MW class output: aerodynamic analysis of stage 1 vane." *Turbo Expo: Power for Land, Sea, and Air*. Vol. 45660. American Society of Mechanical Engineers, 2014.
- [29] Bringer, R. P., and J. M. Smith. "Heat transfer in the critical region." *AICHE Journal* 3.1, 1957, pp. 49-55.
- [30] Krasnoshchekov, E., and Protopopov, V., "Experimental Study of Heat Exchange in Carbon Dioxide in the Supercritical Range at High Temperature Drops," *High Temperature*, Vol. 1, 1966, pp. 375–382.
- [31] Liao, S., and Zhao, T., "An experimental investigation of convection heat transfer to supercritical carbon dioxide in miniature tubes," *International Journal of Heat and Mass*

*Transfer*, Vol. 45, No. 25, 2002, pp. 5025–5034. [https://doi.org/10.1016/s0017-9310\(02\)00206-5](https://doi.org/10.1016/s0017-9310(02)00206-5).

- [32] Liu, Z.-B., He, Y.-L., Yang, Y.-F., and Fei, J.-Y., “Experimental study on heat transfer and pressure drop of supercritical CO<sub>2</sub> cooled in a large tube,” *Applied Thermal Engineering*, Vol. 70, No. 1, 2014, pp. 307–315. <https://doi.org/10.1016/j.applthermaleng.2014.05.024>.
- [33] Filonenko, G. K., “Hydraulic Resistance in Pipes (in Russian),” *Teploenergetika*, Vol. 1, No. 4, 1954, pp. 40–44.
- [34] Lopes, N., Chao, Y., Dasarla, V., Sullivan, N., Ricklick, M., and Boetcher, S., “Comprehensive Review of Supercritical CO<sub>2</sub> Correlations for Straight Tubes: A Historical Perspective,” *Journal of Heat Transfer*, Vol. 144, No. 12, 2022, p. 120801. <https://doi.org/10.1115/1.4055345>.
- [35] Sauerbrun, J., "Design and Characterization of a High pressure Flow Loop for Heat Transfer Experiments of Supercritical Carbon Dioxide," 2023.
- [36] Huber, M., Harvey, A., Lemmon, E., Hardin, G., Bell, I., and McLinden, M., “NIST Reference Fluid Thermodynamic and Transport Properties Database (REFPROP) Version 10 - SRD 23,” 2018. <https://doi.org/10.18434/T4/1502528>.

## 7 PUBLICATIONS

- [1] Velasco, D., Sauerbrun, J. S., Lopes, N. C., Chao, Y., Boetcher, S., and Ricklick, M. A., “Characterization of a sCO<sub>2</sub> Heat Exchanger Flow Loop,” *AIAA SCITECH 2024 Forum, American Institute of Aeronautics and Astronautics*, 2024. <https://doi.org/10.2514/6.2024-2294>.